Quaternary Science Reviews 284 (2022) 107463

Contents lists available at ScienceDirect

Quaternary Science Reviews

journal homepage: www.elsevier.com/locate/quascirev

Using novel methods to track British and Irish Ice Sheet dynamics since the Late Pleistocene, along the west Porcupine Bank, NE Atlantic

Luke O'Reilly [a, *], Aaron Lim [a, b], Jürgen Titschack [c, d], Niamh Moore [e, f], O.J. O'Connor [e, f], John Appah [a], Robin Fentimen [g], Felix Butschek [a, h], Kimberley Harris [i], Torsten Vennemann [j], Andrew J. Wheeler [a, h]

[a] School of Biological, Earth & Environmental Sciences, Environmental Research Institute, Distillery Fields, North Mall Campus, University College Cork (UCC), Ireland
[b] Green Rebel, Crosshaven Boatyard, Crosshaven, Co. Cork, Ireland
[c] MARUM – Center for Marine Environmental Sciences, University of Bremen, Bremen, Germany
[d] Senckenberg am Meer, Marine Research Department, Wilhelmshaven, Germany
[e] Department of Radiology, Cork University Hospital (CUH), Wilton, Cork, Ireland
[f] Department of Radiology, University College Cork, Cork, Ireland
[g] ENS Lyon, Dept of Earth Sciences, Ecole Normale Superieure de Lyon, 46 allée d'Italie, cedex 07, 69364, Lyon, France
[h] iCRAG (Irish Centre for Research in Applied Geosciences), Ireland
[i] DP Energy Ireland Ltd, Mill House, Buttevant, P51 TN35, Co. Cork, Ireland
[j] IDYST – Institute of Earth Surface Dynamics, University of Lausanne, Switzerland

ARTICLE INFO

Article history:
Received 13 December 2021
Received in revised form
1 March 2022
Accepted 15 March 2022
Available online 5 April 2022

Handling Editor: C. O'Cofaigh

Keywords:
Quaternary
North-east Atlantic
Sedimentology-marine cores
Ice-rafted debris
Palaeoceanography
British-Irish ice sheet (BIIS)

ABSTRACT

Extensive research has been undertaken to elucidate the glacial history of the British Irish Ice Sheet (BIIS) in the NE Atlantic. BRITICE-CHRONO has compiled terrestrial and marine based evidence, to provide an empirical reconstruction of ice sheet expansion and retreat during the Late Pleistocene. Across the Irish margin, particular focus has been given to seafloor sediments which contain ice-rafted debris (IRD). However, there are few publications on IRD from areas proximal to the maximum extent of the BIIS, which would offer further insights on the behaviour of the ice sheet during (de)glacial events. Previous exploratory surveys of the west Porcupine Bank (wPB) visually identified IRD on the seafloor and these present a new study site to investigate the extent of the BIIS and the course of its icebergs. Moreover, there are uncertainties about the effects of icebergs on the marine life and cold-water corals occupying the nearby Porcupine Bank Canyon. Assessing a sediment core containing an IRD analogue for the wPB would thus, have a dual purpose. In the past however, coring missions of the wPB using traditional coring methods (i.e. piston and gravity cores) were unsuccessful. Here, we utilized a novel ROV-mounted vibrocoring procedure to capture a 0.75 m IRD-bearing sediment core from the wPB. Then further novel analytical methods (computed tomography-based IRD-detection) were used to quantify IRD every 0.02 cm to provide the highest resolution record of BIIS related IRD to date. From this, several fluxes of IRD deposition onto the wPB between 31.6 and 9 ka BP were revealed and corroborated by other published records from across the NE Atlantic. It was shown that the wPB IRD fluxes occur simultaneously with other parts of the margin. The IRD signal also shows that iceberg calving occurred on the wPB during the Younger Dryas. Grain-size analysis of the core allowed for a reconstruction and interpretation of the palaeoenvironmental conditions during these IRD flux events and shows that BIIS-derived glaciers had a major impact on hydrodynamic conditions in the wPB. Subsequently, intensive scouring led to a major hiatus in the core during 27.3–17.2 ka BP. These results are a useful addition to BIIS literature on this part of the shelf. Furthermore, it shows that bottom currents were influenced by (de)glacial events, an important finding when considering the presence of nearby current-dependant benthos.

* Corresponding author. School of Biological, Earth and Environmental Sciences, University College Cork, North Mall, Cork, T23TK30, Ireland.
E-mail address: lukeoreilly@ucc.ie (L. O'Reilly).

https://doi.org/10.1016/j.quascirev.2022.107463
0277-3791/

1. Introduction

Marine sediments can contain depositional sequences from melting glaciers that provide crucial information for the modelling of former marine-terminated ice-sheets (Boulton, 1996; Ó Cofaigh et al., 2012; Greenwood and Clark, 2009; Rea et al., 2018; Wadham et al., 2019). Understanding the response of these marine-influenced ice-sheets to changes in ocean processes (Andresen et al., 2011; Lloyd et al., 2011) and atmospheric warming (Carr et al., 2013), can provide insights into the responses of larger scale ice masses to changing ocean and atmosphere conditions (Bond et al., 1993). Geomorphological and sedimentological features from the British-Irish Ice-Sheet (BIIS) show an intricate deglaciation history (Clark et al., 2012), which provides an understanding into the response of contemporaneous analogues such as changes to the Greenland Ice-sheet. In recent years, much attention has been given to the sedimentological and geochronological parameters controlling the timing of BIIS retreat during the last glacial-interglacial cycle, e.g. through the BRITICE-CHRONO project (http://www.britice-chrono.org/; see Arosio et al., 2017; Bateman et al., 2017; Bradwell et al., 2019; Callard et al., 2018; Callard et al., 2020; Chiverrell et al., 2018; Ó Cofaigh et al., 2019; Evans et al., 2017; Evans et al., 2019; Evans et al., 2018; Lockhart et al., 2018; Peters et al., 2015, 2016; Praeg et al., 2015; Roberts et al., 2018; Roberts et al., 2019; Scourse et al., 2019; Sejrup et al., 2016; Small et al., 2017; Small et al., 2018; Smedley et al., 2017; Tarlati et al., 2020; Wilson et al., 2018). Along the western Irish Shelf, the BIIS reached its local maximum extent between 29 and 23 ka BP (Ó Cofaigh et al., 2012; Peters et al., 2015) during the Last Glacial Maximum (LGM; Clark et al., 2009). Thereafter, the marine-terminating portion of the BIIS retreated to the northeast until final deglaciation after 15 ka (Clark et al., 2012). However, evidence for episodic readvances in the final stages of BIIS deglaciation in its northerly sectors of the ice mass (Ó Cofaigh et al., 2012; Purcell, 2014) and along the NE Irish Coastlines (Ballantyne and Ó Cofaigh, 2017; McCabe and Clark, 1998), indicated a complex end stage history and it seems numerous re-advancements events remain to be discovered (Peters et al., 2016). Cores taken from areas proximal to BIIS ice stream terminations provide an opportunity for insights into the late history of the BIIS deglacial events in offer such insights in the Rockall Trough (Callard et al., 2018; Georgiopoulou et al., 2012; Roy et al., 2020; Tarlati et al., 2020), the Porcupine Seabight (PS) (Peck et al., 2007; Scourse et al., 2009; van Rooij et al., 2007) and the Goban Spur (Haapaniemi et al., 2010; Hall and McCave, 1998a, b; Scourse et al., 2000).

Within these studies, particular emphasis has been given to the role of ice-rafted debris (IRD) plays in charting the retreat of ice-sheets. IRD is terrigenous material transported within an iceberg from a marine (or lake) terminating glacier and deposited in marine (or lacustrine) sediments as the iceberg melts (Kuijpers et al., 2013) and quantifying IRD in marine sedimentary sequences can provide critical information about the evolution of ice sheets (Andrews, 2000; Kuijpers et al., 2013). Rapidly deposited layers of IRD correspond to periods of abrupt climate change and increased iceberg calving during past glacial cycles, including enigmatic phases of instability such as Heinrich events, Dansgaard-Oeschger cycles or Bond events (Andrews, 2000; Heinrich, 1988; Kuijpers et al., 2013). IRD records from the west coast of Ireland are an established method for reconstructing Pleistocene glacial development (e.g. (Knutz et al., 2001; Owen, 2010; Peck et al., 2006; Peck et al., 2007; Scourse et al., 2009; Tarlati et al., 2020). Sedimentary records from the Porcupine Bank (Owen, 2010; Smeulders et al., 2014) and PS (Knutz et al., 2001; Peck et al., 2006, 2007; Rüggeberg et al., 2005, 2007; Scourse et al., 2009; Thierens et al., 2012; van Rooij et al., 2007) all show episodic delivery of IRD to the seafloor. However, despite extensive research undertaken by BRITICE-CHRONO, there are continuing uncertainties associated with timing and extent of BIIS glacial history on the Porcupine Bank, in particular within areas proximal to the ice sheet.

Explorative surveys of the west Porcupine Bank (wPB) have identified an abundance of IRD and ploughmarks (Lim et al., 2018; Mazzini et al., 2011; Wheeler, 2017) caused by grounded icebergs during glacial sea level low stands (Dorschel et al., 2010). Nearby, the Porcupine Bank Canyon (PBC) incises the shelf, and likely acts as a conduit for glacial and glaciofluvial sediment (Sacchetti et al., 2012). As such, it represents a unique study site to fill current gaps in the understanding of the seafloor proximal to the BIIS. Assessing IRD records from the wPB would in turn enrich the literature on this part of the continental shelf and in particular the PBC which is a documented biological hotspot on the Irish Margin (Appah et al., 2020; Lim et al., 2020). The role of BIIS glaciation on sedimentation and hydrodynamics adjacent to this important habitat remains unclear. Therefore understanding BIIS deglaciation has a twofold purpose. Until now however, conventional coring missions (i.e. piston and gravity cores) have been unsuccessful in the challenging conditions and substrates presented by the wPB (Wheeler et al., 2014).

Thus, the aim of this study is to investigate the ice-ocean interactions on the wPB by utilizing novel coring methods (ROV-vibrocorer). The acquired sediment core was subjected to further novel technologies (computed tomography-based IRD evaluation) to provide a high resolution (0.02 cm) assessment of ice rafted material. From this it was found that IRD was deposited across several flux events since at least 31.6 ka BP. Regional studies are used to interpret climatic signals inferred from the IRD fluxes and their origins. Insights into past bottom and surface water oceanography are constrained from grain-size data and isotopic composition of benthic and planktonic foraminifera. Essentially, this research investigates the glacial history of the BIIS in an area proximal to its maximum extent, building upon current research by BRITICE-CHRONO. In doing so, this study also highlights new techniques in acquiring cores from difficult terrains and shares innovative methods in assessing IRD with the scientific community.

2. Geographical setting

The wPB forms the outermost part of the continental shelf west of Ireland (Fig. 1a) and is part of a N–S trending plateau forming the north-western margin of the PS Basin (Naylor and Shannon, 1975). Part of the wPB is incised by the NE–SW striking Porcupine Bank Canyon (PBC), located roughly 300 km west of Cork, Ireland (Dorschel et al., 2010) (Fig. 1a). It is tectonically controlled (Shannon, 1991; Shannon et al., 2007) and the largest submarine canyon on Ireland's margin. It has three confluent axial channels, each with an axial length of about 60 km (Elliott et al., 2006), which meander along the continental rise and feed into the canyon head (Fig. 1a). High reflectivity in multibeam backscatter data from the north eastern sector of the canyon head shows compacted sands exposed as a result of iceberg ploughmarks (Dorschel et al., 2010; Mazzini et al., 2011) (Fig. 1b insert), which trend mostly NE-SW. Along the interface between the wPB and the PBC, a series of escarpments extend from south to north and are up to 10 km in length and 60 m in height (Mazzini et al., 2011). The coring site is located adjacent to this interface at the eastern canyon flank. The area was recently declared of ecological significance and was designated as a *Special Area of Conservation* under the European Union Habitats Directive (2016). It is home to significant cold-water coral (CWC) habitats (Appah et al., 2020; Dorschel et al., 2010; Lim

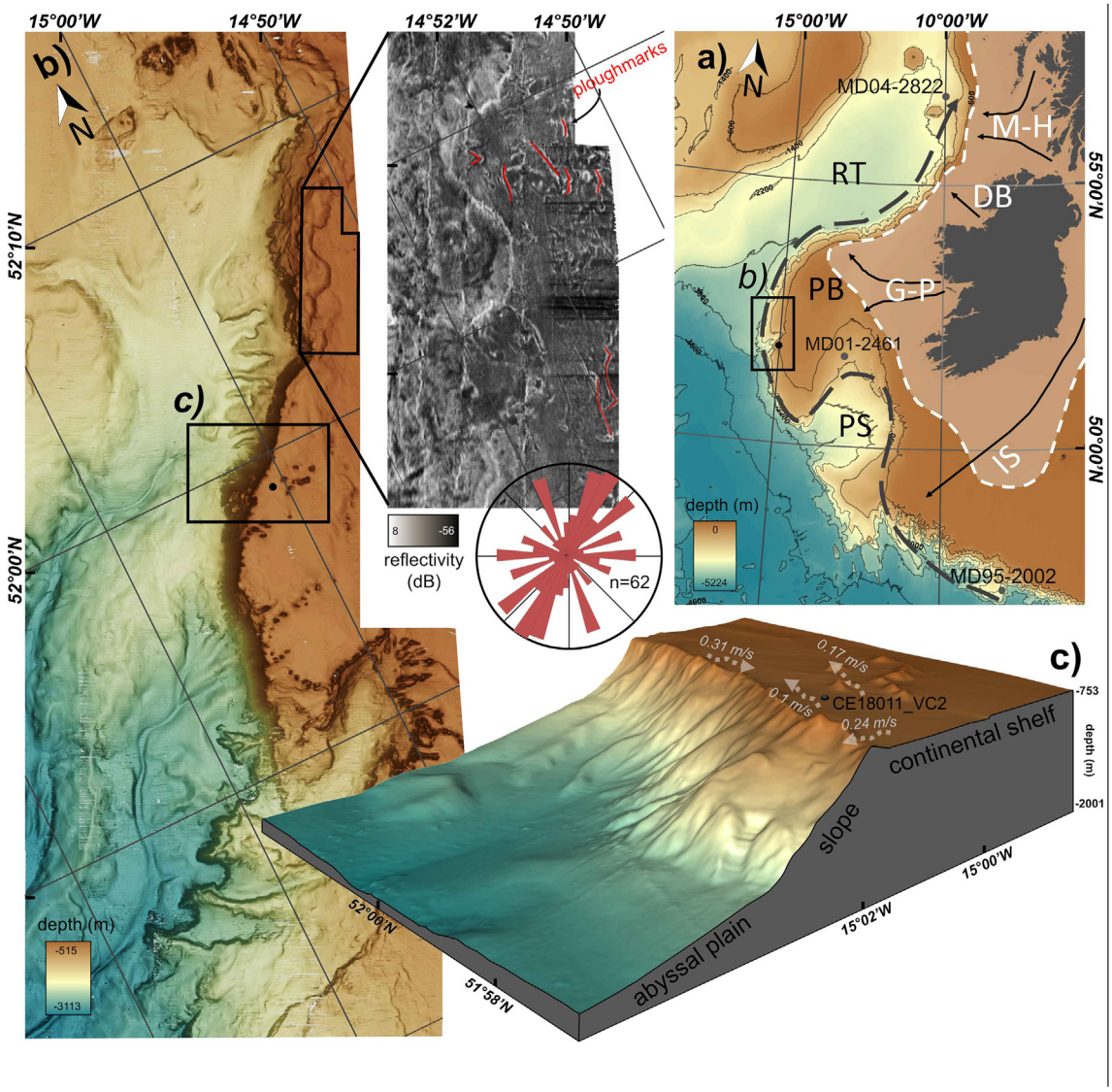

Fig. 1. (a) Location of the study site within the western Porcupine Bank (black rectangle) on the Irish continental margin (PB - Porcupine Bank, PS - Porcupine Seabight, RT - Rockall Trough). White dashed line indicates BIIS maximal extent, based on BRITICE-CHRONO reformulation (after Roberts et al. (2020); Ó Cofaigh et al., 2021. Grey dotted line showing flow direction of Eastern North Atlantic Water which also enters the PS (Wienberg et al., 2020). Black arrows indicate the main ice streams derived from the BRITICE-CHRONO reconstruction described by (Wilton et al., 2021; M-H - Malin-Hebrides, DB - Donegal Bay, G-P - Galway-Porcupine, IS - Irish Sea). Cores mentioned in this study annotated by black dot: MD04-2822 from Knutz et al. (2001), MD01-2461 from (Peck et al., 2006), and MD95-2002 from Toucanne et al., (2015). (b) Bathymetry map of the upper Porcupine Bank Canyon modified after (Lim et al., 2020). Note insert: red lines summarizing several plough marks identified from multibeam echosounder backscatter data. Rose diagram showing ploughmarks orientation (n = 62). (c) Overview of coring site used in this study. Grey arrows show modern day current direction and associated mean current speeds (adapted from Lim et al., 2020). (Maps created using ArcGIS Desktop v10.6 (www.arcgis.com); data sources – (a) - General Bathymetric Charts of the Oceans (gebco.net); (b and c) – additional bathymetry (10 m resolution) collected during CE18011 research cruise (Lim et al., 2018). (For interpretation of the references to colour in this figure legend, the reader is referred to the Web version of this article.)

et al., 2020; Lim et al., 2019b, Lim et al., 2019a; Mazzini et al., 2011), deemed "ecosystem engineers" (Jones et al., 1994).

Eastern North Atlantic Water (ENAW; ~200–700 m water depth) is carried from south to north over the seafloor by a poleward Shelf-Edge Current (Dickson and McCave, 1986; Mazzini et al., 2011; Pollard et al., 1996; White et al., 2007) (Fig. 1a), where the flow becomes locally focussed by positive topographic expressions (Lim et al., 2020). Mediterranean Outflow Water (MOW) exists between 800 and 1000 m water depth. It is characterised by a high salinity (Lim et al., 2020; White et al., 2007) and overlies the denser Labrador Sea Water that occurs at 1100 m water depth (Appah et al., 2020).

3. Methods

3.1. ROV-vibrocorer

Core CE18011_VC2 was acquired from the study site onboard the *RV Celtic Explorer* during the Cold-Water Coral Habitats in Submarine Canyons (CoCoHaCa) II cruise (cruise number CE18011; Lim et al., 2018) using the *Holland I* Remotely Operated Vehicle (ROV) equipped with a vibrocore rig (developed by P&O Maritime and the Marine Institute Ireland). It was retrieved from the seabed adjacent to cold-water coral mounds along the eastern canyon flank on the wPB (depth – 731 m; Fig. 1c). The positioning of the ROV was

acquired through the integration of a Kongsberg HAINS inertial navigation system, ultra-short baseline (USBL) system (Sonardyne Ranger 2) and doppler velocity log (DVL). The core was stored vertically at 4 °C to minimize sediment deformation.

3.2. Core analysis

Non-destructive and destructive multiproxy analytical methods were performed on core CE18011_VC2 to assess relevant paleo-environmental conditions.

3.2.1. Computed tomography

All computed tomography images were acquired using a 64 section Multi-slice scanner (GE Healthcare, Discovery CT 750 HD) at Cork University Hospital, Cork, Ireland. Images were acquired at a slice thickness of 0.625 mm, using 120 kV, 600 mA and a rotation time of 0.8sec, a pitch of 0.984 and a bony convolution algorithm. Images were reconstructed using Model based Iterative Reconstruction (MBIR) Veo (GE Healthcare, GE Medical Systems, Waukesha, WI, USA) with pure iterative reconstruction using a resolution preference of 20% (RP20) increasing the spatial resolution by 20%. An overlapping reconstruction was performed with a final voxel size of 0.195 x 0.195 × 0.625 mm. The original data was recalculated to obtain an isotropic voxel size of 0.2 mm.

Computed Tomography (CT) processing was completed following procedures outlined by (Bartels et al., 2017, 2018) (see also Appendix A). Overlapping IRD volumes were determined for every CT-slice (every 0.2 mm) considering a 51-CT slice window that corresponded to a 1.02 cm interval within the core. Also, the IRD count and the IRD grain-size analyses considered 51 CT-slices. This method was shown to be more effective way of assessing IRD than traditional methods (i.e. hand picking; see Bartels et al., 2017). Reworking by bottom-current can bias IRD concentrations through the selective removal of fines. To counter this potential bias IRD fluxes were calculated (Scourse et al., 2009).

3.2.2. Grain size analysis

Core CE18011_VC2 was frozen at −20 °C and split using an electric circular handsaw, photographed and lithologically described. The matrix sediment composition was determined from 15 samples (every 5 cm) by weight loss after chemical dissolution of the organic matter and carbonate material by following the procedures outlined by Pirlet et al. (2011) (see Appendix B). The siliciclastic matrix fraction was then investigated for grain-size variations. Grains >2 mm were sieved from the samples with a 2 mm sieve. Grains <2 mm were measured using a Malvern Instruments Mastersizer 3000 (MS3000) at University College Cork with a refined standard operating procedure (see Appendix C). The calculated grain-size distribution (GSD) is an average of five total measurements of a sample. This result was used for further statistical analyses in GRADISTAT (see Blott and Pye, 2001) where median grain size (Dx_{50}), mean grain sizes (MGS), kurtosis and sorting were automatically calculated (the latter two using the Folk and Ward method (Folk and Ward, 1957). The mean sortable silt (MSS) was calculated from the differential volume or weight distribution of grains within the 10–63 μm terrigenous silt fraction, following the approach of (McCave and Andrews, 2019). In this study, the MGS and MSS size is used as a proxy to trace changes in near-bottom current strength (McCave et al., 1995b). Stronger bottom-currents yield a coarser mean size of a non-cohesive silt fraction, due to selective deposition and winnowing (McCave et al., 1995b). A calculation of settling velocities further helped to reconstruct bottom-water hydrodynamics (see Soulsby, 1997; (Huvenne et al., 2009; Soulsby, 1997).

3.2.2.1. Grain size end-member modelling. Meaningful sub-populations of GSDs were acquired through end-member modelling algorithms (EMMA) (Prins and Weltje, 1999; Weltje, 1997; Weltje and Prins, 2003). This analysis uses linear mixed modelling to ascertain dominant GSDs which explain the total variation in all GSD, and is a standard approach applied across a range of marine environments (Jonkers et al., 2015; Prins and Weltje, 1999; Prins et al., 2002; Stuut et al., 2007; Thierens et al., 2010; Tjallingii et al., 2008). End-members were determined using the AnalySize MATLAB package version 1.2.0 (available at https://github.com/greigpaterson/AnalySize/releases; (Hateren et al., 2017; Paterson and Heslop, 2015). This approach offers the simplest explanation for the identified variations in GSDs that originated from statistically indistinguishable provenance and/or transport process in each sample (Prins and Weltje, 1999; Weltje and Prins, 2003). The minimum number of EMs were constrained by assessing the coefficients of determination (r^2), which represent the degree of variance present in each grain-size population (Weltje and Prins, 2003). The total % of each EM for a given interval was then plotted versus depth.

3.2.2.1.1. Ground truthing. Ground-truthing the end-members can strengthen the interpretation of the transport mechanisms associated with the grains. In this study, grain surface microtextural analysis were analysed from intervals dominated by EMb to provide provenance and transport information (see Thierens et al., 2010). New methods by Mccave and Andrews (2019b) were followed to determine if a) the lithic fine fraction possesses characteristics of sorting by current, or b) it is an artifact of glacially eroded sediment deposited from melting icebergs that may have fallen through a sluggish water column and deposited on the seafloor relatively undisturbed. As a result, a downcore correlation coefficient was used to separate core intervals dominated by sediments of glacial origin from sediments transported by near bottom currents. Accordingly, a sortable silt percentage (SS%) was calculated by taking the sum weight of the 10–63 μm fraction of the sample divided by the total fine fraction (% <63 μm). A downcore correlation (r_{run}) was then examined between MSS and SS%, whereby r_{run} of <0.5 should be rejected as a proxy for current strength.

3.2.3. AMS radiocarbon measurements

The chronostratigraphy of core CE18011_VC2 is based on 7 accelerator mass spectrometry (AMS) radiocarbon measurements from monospecific samples of the planktonic foraminifera *Globigerina bulloides* taken from the >150 μm aliquot size. Samples were taken from above and below boundaries between sedimentological units (Table 1). The samples were cleaned in an ultrasonic bath prior to submission. At least 15 mg of calcium carbonate was used to acquire each date respectively. The measurements were carried out at DirectAMS Laboratories, Washington, USA. All obtained ages were corrected for ^{13}C and a mean ocean reservoir (ΔR) age of −191 years (±94; Stephen Hopper and Paula Reimer, Queens University Ulster, personal communication, 2021). This ΔR value was calculated using the MARINE20 calibration curve (Heaton et al., 2020) for the west coasts of Ireland, Scotland, Orkney and Outer Hebrides (Reimer et al., 2002), although ΔR could vary through time (Austin et al., 2011). AMS ^{14}C ages were converted to calendar years using the MARINE20 curve (Heaton et al., 2020) of the web-based CALIB7.10 software (Stuiver and Reimer, 1993); http://calib.org/

Table 1
Radiocarbon results for core CE18011_VC2 discussed in this study. Calculated sedimentation rates (SR) also shown.

Lab ID	Depth	Frac. of mod. pMC	^{14}C age		Calibrated age (cal. ka BP)			Bayesian modelled age (ka BP)			SR
	(cm)		[a]	±	μ-2σ	μ+2σ	Median	μ-2σ	μ+2σ	Median	[cm/ka]
D-AMS 038053	7	32.55	9016	37	9.5	10.1	9.8	8.7	9.3	9.0	5.7
D-AMS 038051	17	31.86	9188	45	9.7	10.3	10.0	9.7	10.1	9.9	12.1
D-AMS 039751	26	27.13	10479	41	11.4	12.2	11.8	11.2	11.9	11.6	6.2
D-AMS 038052	33	17.32	14084	51	16.0	16.8	16.4	15.3	16.0	15.7	1.9
D-AMS 039276	41	15.26	15102	63	17.3	18.1	17.7	16.7	17.5	17.1	6.0
D-AMS 034705	48	3.802	26265	114	29.4	30.2	29.8	28.7	29.8	29.3	4.1
D-AMS 034765	59	2.517	29578	252	32.8	34.1	33.4	31.9	33.6	32.8	4.3

calib/calib.html) and reported as kiloyears before present (ka BP, Present = 1950CE).

3.3. Age model

The age model is based on the radiometric dates (Table 1) and was calculated using the R package "rbacon" (Blaauw et al., 2020), which uses Bayesian statistics to reconstruct accumulation history of deposits (Blaauw and Christen, 2011). Sedimentation rates were then determined every 1 cm from the calculated age model. Further information on the parameters used to construct the age model can be found in Appendix F.

4. Results

Analysis performed on core CE18011_VC2, including the core logs, sedimentary and micropaleontological data, CT-scan and geochronology (see section 4.1), are presented against depth to identify weakly bioturbated intervals to help build a chronostratigraphic framework (see section 4.2) and determine major IRD pulses (see section 4.3).

4.1. Description of CE18011_VC2

Core CE18011_VC2 can be divided into 4 lithological units (Fig. 2), based on the different pulse of IRD identified during CT (Fig, 2g). Clear shifts in IRD across unit boundaries can be easily seen in Fig. 2e for Units A, B and C whereas the change is less abrupt between Units C and D. Changes in other variables (Fig. 2g–k) confirm this visual core subdivision. For detailed sedimentological data, see Appendix H.1.

Unit A (48–73 cmbsf)

Unit A (Fig. 2o) is composed of dark brown (Fig. 2c) very poorly sorted (Fig. 2m; average 4.6 μm; see also Appendix H.1) sandy silts and silty sands (Fig. 2l) with a relatively small MGS (Fig. 2i; average 26 μm) and MSS (average 24 μm), with low kurtosis (Fig. 2k; average 0.83). Unit A also showed a low σMSD (Fig. 2h). Settling velocities calculated for this interval are relatively fast (Fig. 2j; average 0.37 ms^{-1}).

CT scanning revealed two high x-ray density intervals within Unit A, visible at 57–60 and 52–54 cmbsf (Fig. 2b), that show sharp contacts to the underlying lower density sediments. The lower sections of this unit (i.e. 60–73 cmbsf) also had a high-density signature with minor pockets of lower density sediments throughout (see also Fig. 2b and c). Minor peaks in standard deviation in matrix sediment density (σMSD; Fig. 2h) are visible at 62 and 51 cmbsf. Bioclastic material is observed in trace amounts (Fig. 2d). Between 66 and 73 cmbsf, IRD clasts are abundant (up to 31 clasts/cm^3; Fig. 2g). Moderate amounts (up to 11 clasts/cm^3) of IRD are visible in the remainder of the unit. Vol. % of IRD in Unit A (Fig. 2g) occurs continuously throughout the unit, but several pulses are seen peaking at 71 (7.8 vol%), 63 (5 vol%) and 50 (4 vol%) cmbsf. A large sub-cm clast is present at 63 cmbsf.

Unit B (42–48 cmbsf)

Unit B (Fig. 2o) is composed of dark brown (Fig. 2c) poorly sorted (Fig. 2m; 3.3 μm; see also Appendix H.1) silty sands (Fig. 2l) with relatively small MGS (Fig. 2i; 12 μm) and small MSS (Fig. 2i; 21 μm), with a high kurtosis (Fig. 2k; 1.1). Unit B also showed a low σMSD (Fig. 2h). Settling velocities calculated for this interval are slow (Fig. 2j; 0.23 ms^{-1}).

Unit B recorded a low X-ray density unit with a dewatering fracture from core recovery visible at its top (Fig. 2b). Bioclastic material is abundant within Unit B (Fig. 2d). IRD clasts are present in trace amounts (Fig. 2g; <3 clasts/cm^3; <0.2 vol%). At the top of Unit B, an erosive boundary is visible (Fig. 2b and c).

Unit C (18–42 cmbsf)

Unit C (Fig. 2o) is composed of very poorly sorted (Fig. 2m; average 4.7 μm; see also Appendix H.1) sandy silts and silty sands (Fig. 2l). The sediment colour composition progresses from dark brown to very dark greyish brown at 33 cmbsf (Fig. 2c). It has a relatively large MGS (Fig. 2i; average 36 μm) and moderate MSS (Fig. 2i; average 26 μm), with a low kurtosis (Fig. 2 k; average 0.85). Settling velocities calculated for this interval are relatively fast (Fig. 2j; average 0.38 ms^{-1}).

Unit C recorded variable X-ray density, whereby in the lower sections (Fig. 2b; between 30 and 42 cmbsf), the sediment appears to become more heterogenous, with the less dense sediments (dark grey) becoming mixed with the denser sediments (light grey). This interval also showed a high σMSD (Fig. 2h). Contrastingly, the upper section of the unit becomes more homogenous with low σMSD. A dewatering structure is visible at 32 cmbsf. The base of the unit is an erosive boundary (Fig. 2b and c). Bioclastic material is abundant between 28 and 42 cmbsf, and is mostly composed of angular shells, but a scaphopod and gastropod are also present (Fig. 2d). IRD in Unit C occurs continuously throughout the unit (average 7 clasts/cm^3; Fig. 2g). Large sub-cm clasts influence several pulses in IRD vol % seen at 40 (3.5 vol%), 32 (3.9 vol%), 24 (6.6 vol%) and 21 (2.5 vol%) cmbsf.

Unit D (0–18 cmbsf)

Unit D (Fig. 2o) is composed of very dark greyish brown (Fig. 2c) very poorly sorted (Fig. 2m; average 4.3 μm; see also Appendix H.1) sandy silts. The unit has a relatively moderate MGS (Fig. 2i; average 26 μm) and moderate MSS (average 24 μm), with a low kurtosis (Fig. 2k; average 0.95). Settling velocities calculated for this interval are relatively moderate (Fig. 2j; average 0.31 ms^{-1}).

Unit D recorded high X-ray densities with pockets of lower

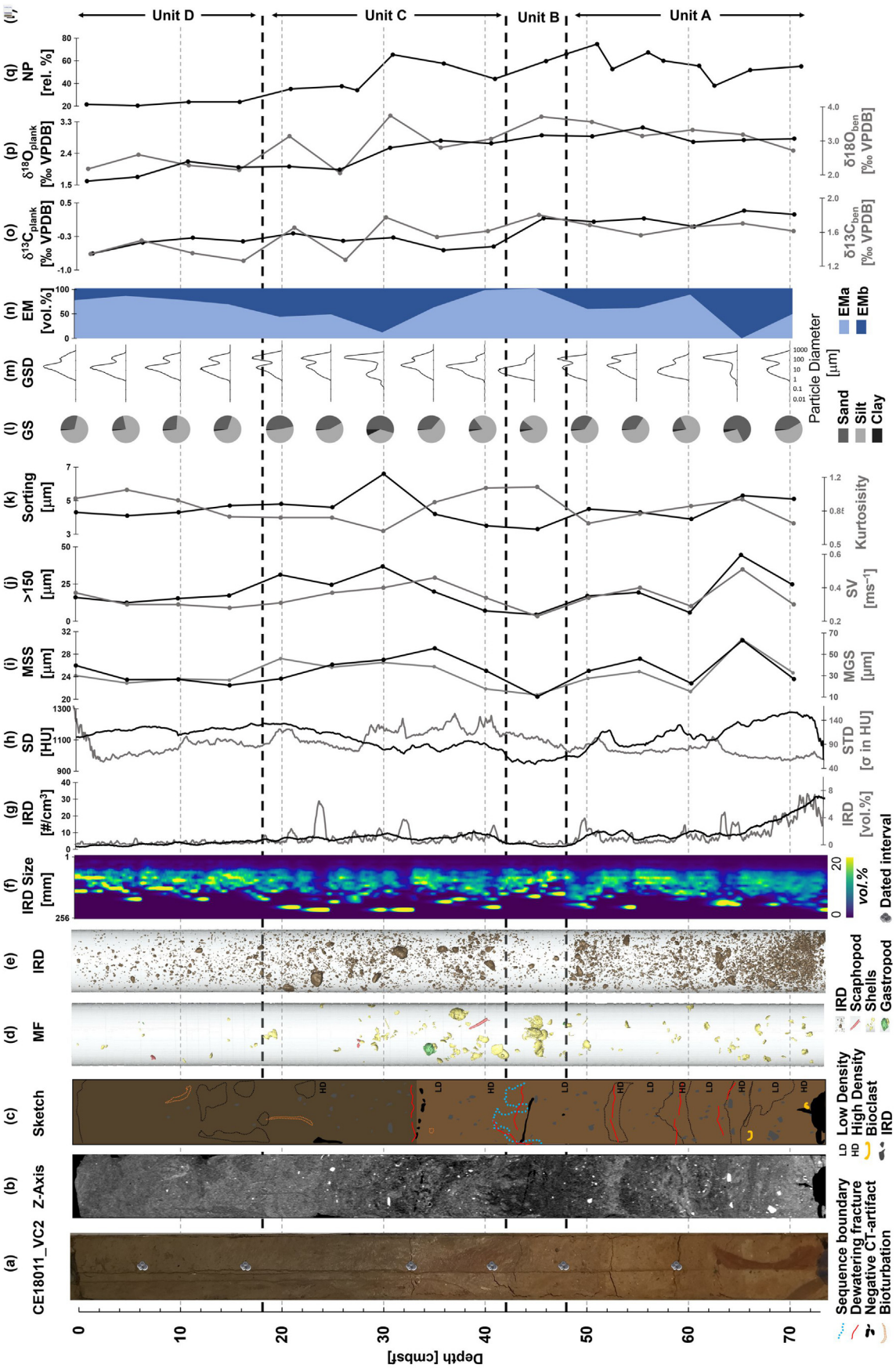
Unit D
Unit C
Unit B
Unit A
(a) CE18011_VC2
(b) Z-Axis
(c) Sketch
(d) MF
(e) IRD
(f) IRD Size [mm]
(g) IRD [#/cm³]
(h) SD [HU]
(i) MSS [µm]
(j) >150 [µm]
(k) Sorting [µm]
(l) GS
(m) GSD
(n) EM [vol.%]
(o) δ13Cplank [‰ VPDB]
(p) δ18Oplank [‰ VPDB]
(q) NP [rel. %]
δ18Oben [‰ VPDB]
δ13Cben [‰ VPDB]
EMa
EMb
Particle Diameter [µm]
Sand
Silt
Clay
Kurtosisity
SV [ms⁻¹]
MGS [µm]
STD [σ in HU]
IRD [vol.%]
vol.%
Dated interval
IRD
Scaphopod Shells
Gastropod
Low Density
High Density
Bioclast
IRD
Sequence boundary
Dewatering fracture
Negative C1-artifact
Bioturbation
Depth [cmbsf]

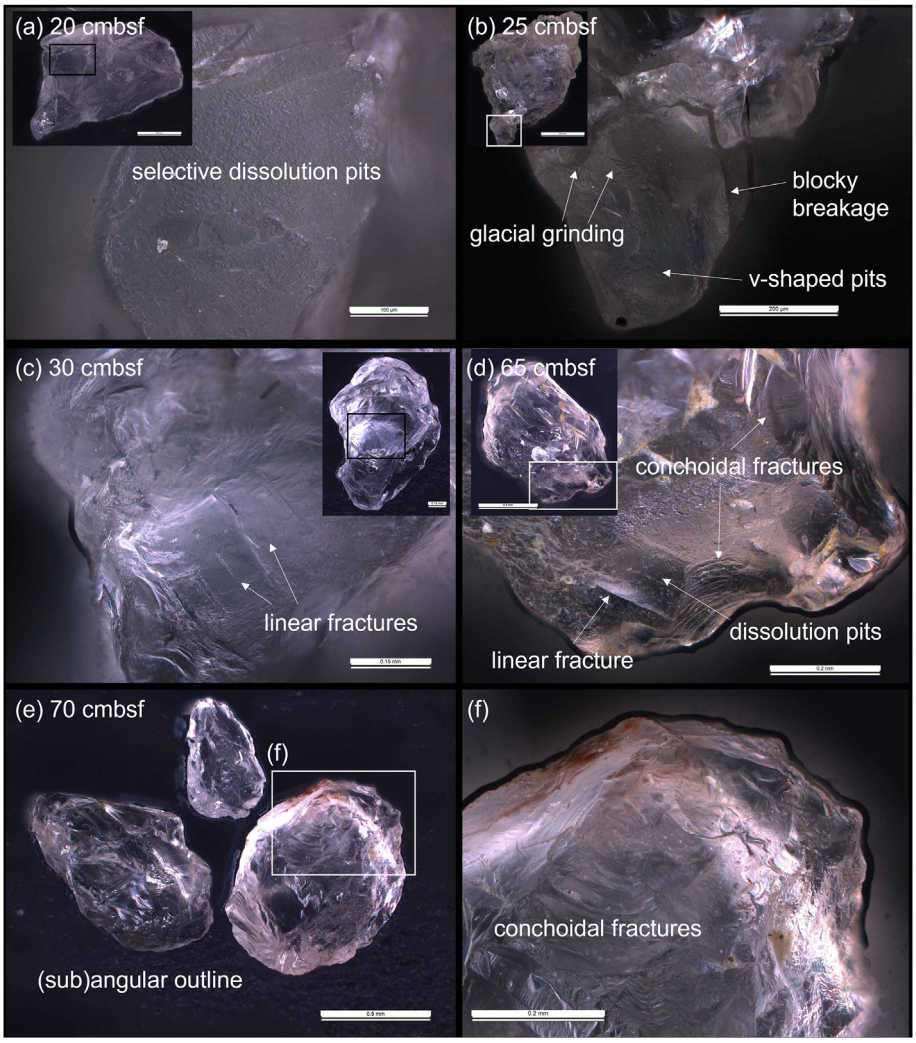

Fig. 3. Surface microtextures identified in EMb dominated intervals.

density sediment (dark grey circles) and vertical stratification visible between 12 and 18 cmbsf (Fig. 2c and d). A minor amount of bioclast material is present (Fig. 2d). IRD clasts are present in trace amounts (Fig. 2g; <3 clasts/cm^3; <0.5 vol%).

4.1.1. End-member modelling analysis

End-member modelling identified two meaningful sub-populations of GSDs (Fig. 2n, Appendix D). The relative strength of these end-members, EMa and EMb, describe the changes in down-core grain-size variation with a high R^2 value accounting for 92% of the variance seen in CE18011_VC2 (Appendix D; section b). Adding a third end member increases the variance captured to 98%, although it increases the risk of modelling noise rather than signal (Thierens et al., 2010). Therefore, two end members were considered as reliable. The principal GSDs of EMa are centred around a mean of 14 μm and a mode of 19 μm, whereas EMb is centred around a mean of 59 and a mode of 163 μm (Appendix D; section d). Core VC18011_VC2 is dominated by EMa (Fig. 2n). Two minor layers are EMb dominated, seen in the lower part of Unit A at 65 cmbsf and the upper part of Unit C at 30 cmbsf.

4.1.1.1. Ground truthing. A downcore correlation of MSS and SS% of the fine fraction obtained a value of 0.1. However, upon the removal of two outliers (from 30 to 65 cmbsf, both which showed more of a preference to EMb) a value of 0.6 was recorded (see Appendix D).

20 sand-sized quartz grains were selected at random from intervals dominated by EMb and subsequently investigated using a digital light microscope. In general, evidence of mechanical abrasion was identifiable across each of the grains from these intervals (Fig. 3a–e), including conchoidal fractures, block breakage, glacial

Fig. 2. a-o Compiled computed tomography (CT), sedimentology and microfossil data of core VC18011_VC2 plotted versus depth in centimetres below seafloor (cmbsf). Units A–D identified following multiproxy assessment of core. (a) true-colour image of core; (b) orthogonal CT-image of core, with darkness a function of density. Note: IRD throughout (high density; white); (c) sketch log interpreted from x-ray; (d) 3D image of bioclasts identified in core (see legend for bioclast types); (e) 3D image of ice-rafted debris (IRD) content; (f) IRD clast size distribution (0–20 vol% of clasts: blue to red, respectively); (g) Number of IRD clasts per cm^3 (black) and vol% of IRD (grey) derived from CT data; (h) Sediment density (black; see Appendix A) and standard deviation sediment density (grey); (j) Mean sortable silt size (black) and mean grain size (grey); (k) vol% of sediment >150 μm (black) and settling velocities (ms^{-1}; grey); (l) kurtosity sand, silt and clay percentages shown as pie charts, centred at appropriate depth intervals; (m) grain-size distributions of siliciclastic sediments; (n) End Member dominance calculated for each grain size distribution; (o) inferred boundaries between units. (For interpretation of the references to colour in this figure legend, the reader is referred to the Web version of this article.)

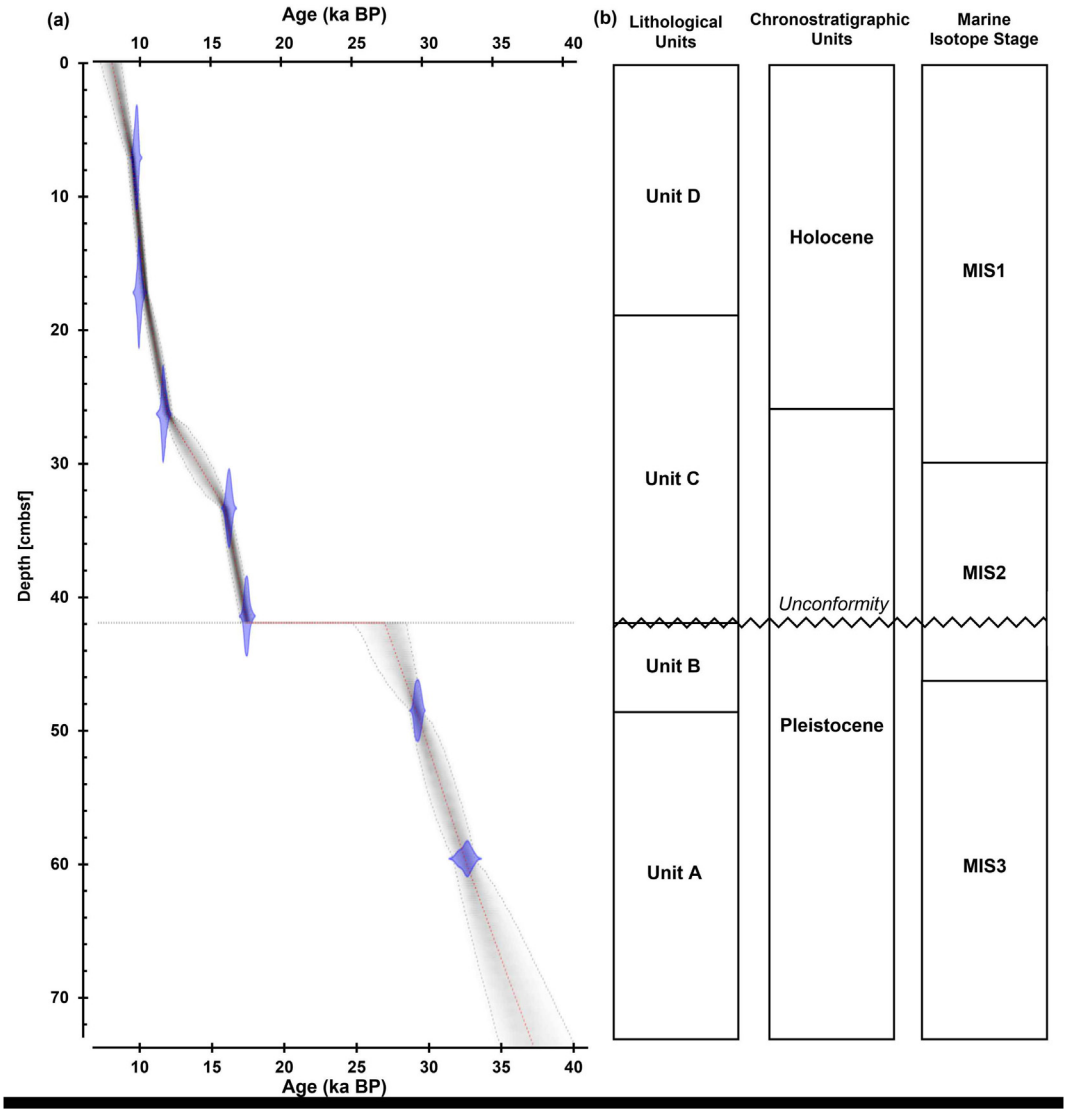

Fig. 4. (a) Age model established with RBacon using 7 AMS ^{14}C dates. (b) Subsequent classification of core CE18011_VC2 versus depth.

grinding and crushing. Moreover, solution pits were also identifiable in places (Fig. 3a). Grains were typically angular to sub-angular in size and had high relief.

4.2. Chronostratigraphic framework

The chronostratigraphic framework of the core VC18011_VC2 is constrained by seven AMS ^{14}C ages, which range between 33.4 ka BP (at 59 cmbsf) and 9.8 ka BP (core top at 7 cmbsf; see Table 1).

4.2.1. Age model development

The age model was clipped at the oldest and youngest dated boundaries. However, estimates determined by the model past the limits of these ages are visible in Fig. 4a and Fig. 5. The age model (Fig. 4a) shows that the constrained section of the core spans an interval of about 9–32.8 ka BP, with an unconformity present from 27.3 to 17.2 ka BP (at 42 cmbsf). Outside the limits of the age model, the core spans from 37.6 to 7.6 ka BP. Consequently, Unit A spans from older than 32.8 ka BP to 29.3 ka BP, Unit B spans from 29.3 to 27.3 ka BP, Unit C spans from 17.2 to 10.1 ka BP and Unit D spans from 10.1 ka BP to younger than 9 ka BP.

4.3. Sedimentation rates and ice rafted debris events

Maximum sedimentation rates reach 6 cm/ka during the Late Pleistocene, which increases to 12.1 cm/ka during the Holocene (Table 1). The CT imagery of core CE18011_VC2 shows the prevalence of large and varying concentrations of IRD clasts (Fig. 2f). During the Late Pleistocene, IRD flux shows that IRD is deposited in events (Fig. 5c). Below the oldest dated interval at 32.8 ka BP, IRD decreases steadily from 37.6 to 34.1 ka BP from 113 to 48 cm^{-2} yr^{-1}. Following this, a brief peak IRD flux occurs at 33.7 ka BP (50 cm^{-2} yr^{-1}). IRD flux decreases to 25 cm^{-2} yr^{-1} until 32.9 ka BP. Within the constrained section of the core, the oldest flux peak event occurs at 32.5 ka BP (40 cm^{-2} yr^{-1}). Two peaks additional are centred 31.4 ka BP (50 cm^{-2} yr^{-1}) and 30.7 (48 cm^{-2} yr^{-1}). IRD flux decreases rapidly to 6 cm^{-2} yr^{-1} until 29 ka BP. Following this low occurrence of IRD flux, it then increases rapidly to 34 cm^{-2} yr^{-1} until the base of the unconformity at 27.3 ka BP (Fig. 5). At the top of the unconformity, a peak in IRD flux is visible at 16.9 ka BP (65 cm^{-2} yr^{-1}). IRD flux decreases steadily to 30 cm^{-2} yr^{-1} until 15.7 ka BP. The period of low IRD flux (maximum flux rates - 17 cm^{-2} yr^{-1}; minimum flux rates 9 cm^{-2} yr^{-1}) correlates with low

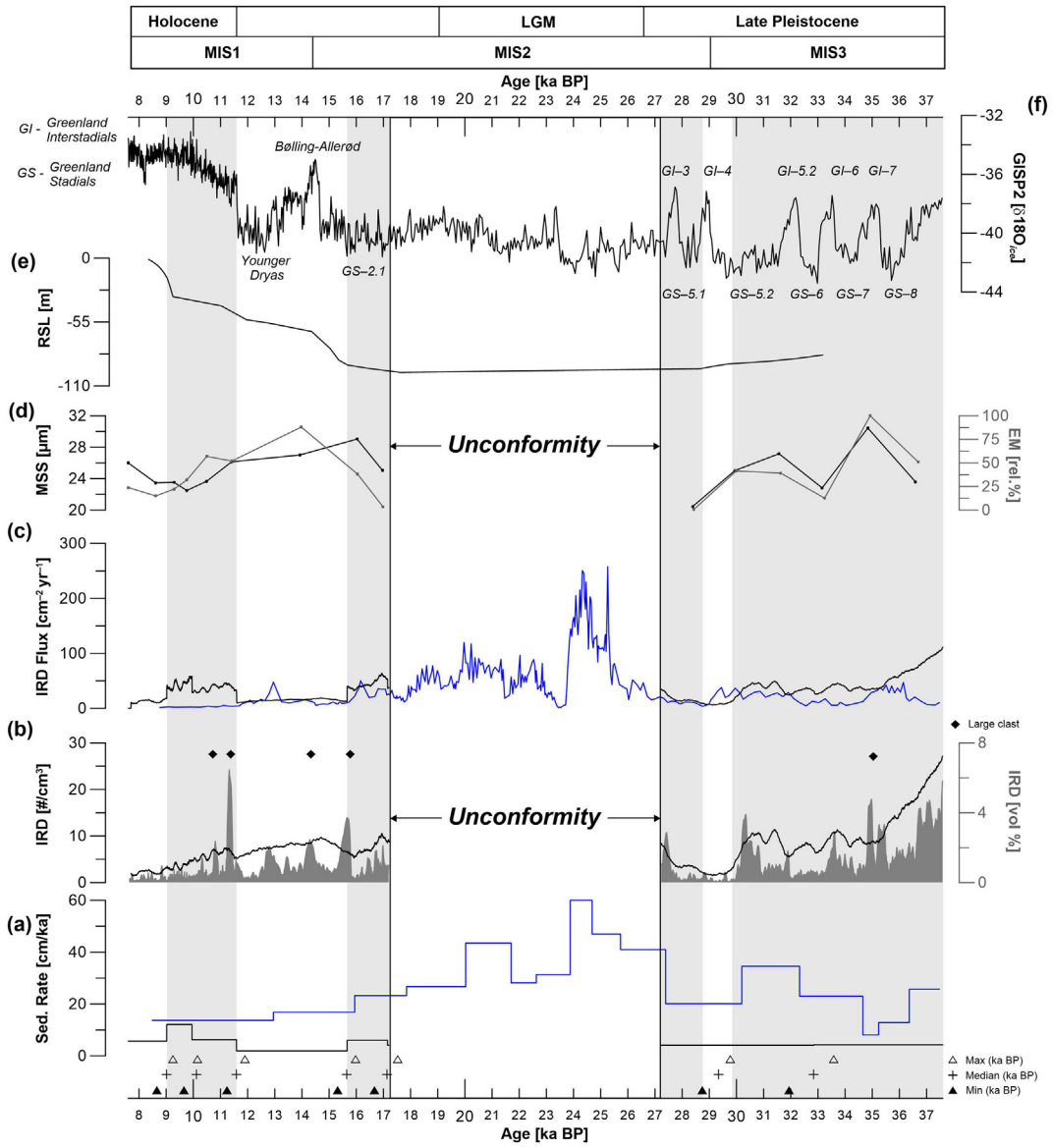

Fig. 5. Compilation of multi-proxy data obtained from core VC18011_VC2 (in black and grey) plotted against time. Includes an unconformity from 27.3 to 17.2 ka BP. Periods containing high IRD fluxes are shown as shaded grey areas. Modelled ages (in kiloyears BP) at bottom are annotated by black cross (median), white triangles (maximum) and black triangles (minimum). The data of Peck et al., (2006) from the Porcupine Seabight is also shown (in blue). To exclude any potential offsets, the data set was recalibrated using the MARINE20 calibration curve (Heaton et al., 2020). (a) sedimentation rates; (b) IRD volume percentage (solid black line), IRD clasts per cubic centimetre (light grey filled in); (c) IRD flux; (d) Mean sortable silt (SS - black) and relative percentage of end members (grey), whereby 0% represents an end member composed entirely of EMa and 100% represents an end member composed of EMb; (e) Relative sea-level estimates in metres were calculated from models composed by (Brooks et al., 2008) and was simulated by the glacial rebound model of Bradley (2011) and applied to the area (personal communication Robin Edwards, Trinity College Dublin, 2021); (f) GISP Greenland Ice Core $\delta^{18}O$ values. (For interpretation of the references to colour in this figure legend, the reader is referred to the Web version of this article.)

sedimentation between 15.7 and 11.6 ka BP (1.9 cm/ka; see Table 1 and Fig. 5). During the Holocene, several minor IRD flux peaks are visible centred at 11.2 ka BP (46 cm^{-2} yr^{-1}), 10.7 ka BP (43 cm^{-2} yr^{-1}) and 10.3 ka BP (38 cm^{-2} yr^{-1}). Between 9.9 and 9 ka BP, sedimentation rates peak (12.1 cm/ka). Contemporaneous with this, three IRD flux peaks are visible at 9.9 ka BP (60 cm^{-2} yr^{-1}), 9.6 ka BP (56 cm^{-2} yr^{-1}) and at 9.0 ka BP (42 cm^{-2} yr^{-1}). IRD flux then remains low until the top of the core (maximum flux rates - 17 cm^{-2} yr^{-1}; minimum flux rates 8 cm^{-2} yr^{-1}). Visual inspection of sediment grains >150 μm from these pulses show diagnostic features of glacial crushing (Fig. 3).

5. Discussion

This study is the first to utilize the *Holland 1 ROV* vibrocoring rig, allowing users to precisely target coring sites, through the use of front facing cameras and sonar on the ROV. For this study, it was essential to core through surface sediments which had not undergone scouring, and to uncover the cause of the ploughmarks identified in the backscatter data. Core records elsewhere on the PB (<50 km north of the site), show an enhancement of currents correlating with interstadial warming during MIS2 (Øvrebø et al., 2006), that resulted in the winnowing of older stadial deposits.

Novel ROV-assisted vibrocoring techniques used in this allowed sampling of CE180011_VC2 from one of the least hydrologically inactive areas of the wPB and adjacent canyon setting (average speeds of 0.1 m s^{-1}; Lim et al., 2020). This area is considered too far from local control of bathymetric features (i.e. carbonate mounds and the submarine canyon) that intensify currents in the region, and instead is influenced by regional processes such as the northerly flowing ENAW (Lim et al., 2020). Moreover, coring in sandy substrate with traditional coring units (i.e. gravity and piston coring) can prove difficult, a testament of which is outlined through previous coring missions in this part of the NE Atlantic (e.g. Wheeler et al., 2014).

The collected core was subjected a non-destructive CT-based IRD analysis that allows the assessment of IRD >1 mm every 0.02 cm with their number/volume, their relative volume and their size distribution (Fig. 2d–f). The traditional method of IRD quantification ("picking") may miss crucial boundaries between IRD pulses. The implementation of CT based IRD detection and quantification can further constrain these time periods and synchronise NE Atlantic IRD reconstructions. Additionally, grain-size analysis and end-member modelling analysis reveal how hydrodynamics on the wPB were influenced by BIIS (de)glaciation.

5.1. Sedimentology

CT scanning reveals that core CE18011_VC2 is composed of four broad lithostratigraphic units based on the presence of IRD (Fig. 2). Grain-size analysis of the core shows that it is composed of either poorly sorted sandy silts or silty sands (Fig. 2l). Mean sortable silt values and calculated settling velocities show that the wPB maintained high current speeds throughout the Late Pleistocene and Early Holocene (minimal calculated velocity is 0.23 m s^{-1}; Fig. 2i and j). The presented age model suggests that sedimentation rates were higher in the Early Holocene than in the Late Pleistocene (Fig. 5), with the top and bottom sections of the core estimated to be younger than 9 ka BP and older than 32.8 ka BP in age, respectively. The diagnostic feature of this core is its IRD record, which occurs in pulses (Fig. 2e; Fig. 2f). Throughout the core, IRD clast sizes typically range between 5 and 7 mm (Fig. 2f; see data availability). Several sub-cm clasts were also identified during this investigation (Fig. 2e). Finally, an erosive boundary was identified between Units B and C (Fig. 4).

5.1.1. What are the causes of the IRD pulses?

Icebergs present an important source of glacial sediment in marine records, which can be transported hundreds of km from the ice margin (deGelleke et al., 2013; Syvitski et al., 1996). An abundance of IRD pulses have been captured throughout core CE18011_VC2 (Fig. 2f) and show depositional similarities with records from other glaciated margins across the NE Atlantic (Peck et al., 2006, 2007; Scourse et al., 2019; Tarlati et al., 2020). Grains identified within these events are overall angular to sub-angular in shape, suggesting this material was abraded by reworking or current transport. Surface microtextures identified on quartz grains (Fig. 3), including conchoidal fracturing, provides evidence for glacially-induced mechanical abrasion, caused by ice transport (e.g. (Cowan et al., 2008; Damiani et al., 2006; Eldrett et al., 2007; Helland and Holmes, 1997; Mahaney, 2002; Mahaney and Kalm, 2000; Woronko, 2016; Wu et al., 2020), confirming glacial origins. However, the IRD pulses captured and what they represent, can be difficult to decipher due to a number of regional controls (for instance the rate and trajectory of calving icebergs; ocean and ice temperature; see Scourse et al., 2009). Local controls, including bioturbation and winnowing can also overestimate the amount of IRD in certain sections of a geological core. Additionally, an absence of IRD deposition does not necessarily translate to a period where icebergs were not along the wPB (i.e. within Units C and A; Fig. 2e). Furthermore, where IRD *is* present, this does not mean a complete deglaciation occurred (i.e. within units D and B). All these factors play a part in concealing true ice rafting events within the IRD pulses identified within this study. However, integrating our records with IRD records from nearby localities can be used to interpret these signals correctly.

5.1.1.1. Pre-Last Glacial Maximum.

At least five peaks in IRD clasts/cm^3 and volume% occur prior to the LGM (Fig. 5b). One non-constrained by the age model and are centred at 33.7 ka BP. The remaining four events are constrained and are centred at 32.5, 31.4, 30.7 and 27.3 ka BP (Fig. 5b) are marginally greater to the PS (Fig. 5c). Other IRD depositional records also show this millennial-scale IRD cyclicity starting from 45 ka BP (Knutz et al., 2001; Peck et al., 2007; Scourse et al., 2009). Several authors attributed these cycles to Dansgaard-Oeschger cycles (Haapaniemi et al., 2010; Knutz et al., 2001; Peck et al., 2006; Scourse et al., 2009; Wilson and Austin, 2002; Wilson et al., 2002) that occur on a periodicity of roughly 1.5 ka (Schulz, 2002). This atmospheric warming could be a key function in the calving of icebergs during this time, and result in IRD deposition along the Irish margin, including the wPB. Observational data suggests that these icebergs originated largely from the Malin Sea Ice Stream but may also have a minor contribution from the Irish Sea and Donegal Bay Ice Streams (Benetti et al., 2021; see also Purcell, 2018), controlled by the bifurcation between the sub-polar and subtropical gyres (Purcell, 2018) coupled with the millennial meridional migration of the North Atlantic Polar Front (Scourse et al., 2009). In contrast, recent studies show that the Galway-Porcupine Lobe was a major drainage pathway for icebergs (Callard et al., 2020; Ó Cofaigh et al., 2021) and thus, may be dominant source of IRD to the wPB. However, no evidence has been found that icebergs from this sector followed a dominant steam (i.e. the Galway-Porcupine Ice Steam; see Wilton et al., 2021). As such, our records would be well suited to a future provenance study to identify the source(s) of IRD through time.

5.1.1.2. Post-Last Glacial Maximum.

Sedimentation resumes above the unconformity occurs following a 10.1 kyr long hiatus (27.3–17.2 ka BP). Fluxes in IRD are observed between 17 and 15.7 ka BP (peaking at 16.9 ka BP) and are again marginally higher when compared to the PS during this time. Simultaneous IRD peaks have also been observed in the Rockall Trough (16.9 ka BP; see Tarlati et al., 2020) and as far afield as the Bay of Biscay (16.7 ka BP; see Toucanne et al., 2015). Offsets of a few hundred years between the sites could be due to differences in proximity to the BIIS combined with uncertainties in the age models and calibration curves used (i.e. MARINE20 curve; see Heaton et al., 2020).

Following this event, IRD flux remains low between 15.7 and 11.6 ka BP during the Bølling–Allerød interval, despite IRD abundances remaining relatively high (Fig. 5b and c). During this time, sedimentation rates are low (1.9 cm/ka) perhaps suggesting there may have been a period of non-deposition or strong bottom currents. During intervals between pulses of icebergs, winnowing is likely to have taken place where currents become intensified, concurrent with other parts of the margin (Øvrebø et al., 2006). A large error is attributed to these sediments within the age model (Fig. 4a), supporting this further. Thus, IRD abundances for this period will be greatly overestimated (i.e. Fig. 5b). Icebergs which deposited this material likely sourced from the Celtic Sea Ice Stream (Purcell, 2018).

Holocene IRD fluxes are suspect (Fig. 5c). With the exception of Bond et al. (1993), no other regional records show such events through this period. Thus, ages which constrain this period are

erroneously young and are possibly better represented by their maximum calibrated ages that tie the event down to 12.7–9.3 ka BP (Fig. 5; see also Table 1). Considering environmental modifications to these sediments supports this forced readjustment. Lower density pockets of sediment and vertical stratifications were noted throughout Unit D (Fig. 2b and c), as well as a minor increase in the standard deviation in matrix sediment density (Fig. 2c and h; see also Appendix G section i) suggests partial mixing by burrowing organisms (i.e. bioturbation) causing an age reversal. This, alongside low confidence in the topmost dates, lead us to postulated that this IRD event is part of the Younger Dryas (YD) flux event recorded in the PS (Fig. 5c) and the Porcupine Trough (12.9 ka BP; Tarlati et al., 2020), marking the conclusion of large-scale iceberg melting and the ultimate retreat of the BIIS. Crucially, this demonstrates that active calving margins were present on the wPB during the YD.

In summary, NE Atlantic IRD capture the release of icebergs during BIIS deglaciation along with the landward retreat of the ice sheet margin (Clark et al., 2012), including proximal areas (i.e. the wPB). IRD supply to the wPB occurred more or less synchronously to other NE Atlantic localities throughout this period. High fluxes of IRD punctuating this deposition are interpreted as a function of mixed calving events and the presence of icebergs originated from the Donegal-Malin Ice Stream (see Purcell, 2018) or from the Galway-Porcupine Ice Stream (see Wilton et al., 2021). Nearby ploughmarks strike mostly NE-SW (Fig. 1b insert), suggesting longshore transport of icebergs occurred, which would favour the observational based origins Donegal-Malin Ice Stream origin (e.g. Purcell, 2018). Equivalently, these ploughmarks could still be caused from Galway-Porcupine icebergs, which may have undergone a sharp change in drift direction towards the wPB (James Scourse, personal communication, 2021).

5.1.2. The impacts of glaciation on background sedimentation

Sediments on the wPB are likely to be from cross slope and upwelling currents related to the PBC (Lim et al., 2020). The correlation between MSS and SS% (Fig. 4) confirms that the fine fraction of this sediment reflects predominantly hydrodynamics and changes in current strength. Two outliers removed from the correlation were extracted from peak IRD intervals and each showed evidence of extensive glacial crushing. The dominance of EMa (Fig. 5d) and low modes reported in the GSD (Appendix H.1) during glacial periods, provide evidence that sediments are locally sourced (and sorted) by relatively weaker bottom currents. Recent paleotidal simulations show that the glaciated NE Atlantic was megatidal (Scourse et al., 2018). As such, tidal pumping may have a control on bed stresses at >700 water depth, further driving sorting processes (e.g. (Woodworth et al., 2019) and references therein) on the wPB.

By comparison, during interglacial and glacial interstadial phases, EMb dominates (Fig. 5d). Surface microtextures on quartz grains (Fig. 3) confirm that each occurrence of this EM has glacial provenance. These sediments also have considerable amounts of fine IRD (i.e., >150 μm; Appendix G section d), highlighting the dominance of iceberg sediment supply to the area during warming phases. The wPB is a considerable distance to the end-moraines captured on the PB (e.g. Peters et al., 2015; Peters et al., 2016; Ó Cofaigh et al., 2021), thus plumites are an unlikely source of this material.

Generally, the sections of the core that align with periods of minimised IRD deposition show a preference to EMa and an increase in sedimentation rate. In contrast, IRD pulses are synchronous with the dominance of EMb and low sedimentation rates. These observations are consistent with interpretations from the nearby PB with interglacial sediments consisting of hemipelagic sediments with little to no IRD, whereas glacial sediments are characteristically IRD-rich fine-grained muds and clays. (Øvrebø et al., 2006; Øvrebø and Shannon, 2005).

5.2. The impacts of (de)glaciation on hydrodynamics

Mean grain size data of the non-carbonate sortable silt is an established proxy for paleocurrent strength (McCave et al., 1995b). The validity check introduced by Mccave and Andrews (2019) showed that sortable silt on the wPB provides reliable current vigour estimates (although note that Weiser et al. (2021) pointed out that the validity check should be used with caution). As such, changes observed in current velocity are reflected temporally by grain size data.

Assuming peaks in MSS at 35 and 30.5 ka BP correspond to GI–7 and GI–5.2 (Fig. 5d), it is inferred that subsequent calculated current velocities are higher during interstadial/warming periods. These peak current velocities (0.51 and 0.40 ms^{-1}) are high enough to cause erosion and winnowing of clay and silt sizes (e.g. Black et al., 2003; van Ledden et al., 2004; Jacobs et al., 2011), ultimately overestimating the coarser fraction of the GSD. Present day current speeds measured from this site are generally slow (mean = 0.09 ms^{-1}), however short pulses of strong currents (0.34 ms^{-1}) are also observed (Lim et al., 2020). Such pulses would also be adequate in removing finer material. GSD from the GI–7 high velocity event shows a positively skewed tri-modal distribution (Fig. 2m), evidence that the removal of finer material has occurred (see McLaren, 1981). This GSD was also identified as an outlier when ground truthing the end-members (Appendix E). On the basis of its GSD, the GI–5.2 high velocity event remains valid and should be considered representative of current speeds (0.40 ms^{-1}) during Late Pleistocene interstadial phases. Lower current speeds recorded between these higher velocity events may thus be likely to correspond to stadial phases such as at 36.4 ka BP with GS–8 (0.30 ms^{-1}), 33.1 ka BP with GS–6 (0.29 ms^{-1}) and at 28 ka BP with GS–5.1 (0.23 ms^{-1}). This sluggish nature of glaciated currents can be linked to the deceleration of North Atlantic currents, resulting from the freshwater release from melting ice-sheets (Bigg et al., 2012; Øvrebø et al., 2006; Stanford et al., 2011; Toucanne et al., 2015) and a reduction in current speeds and internal waves and tides between the ENAW and MOW (Dorschel et al., 2005; Manighetti and McCave, 1995a, b; McCave et al., 1995a; McCave et al., 1995b).

5.3. Explanation of the hiatus

An erosive boundary was identified in core CE18011_VC2 (Fig. 2c) between lithological Units B and C at 41cmbsf. The age model presented in this study suggests that 10.1 kyr worth of depositional record was missing between 27.3 and 17.2 ka BP (Fig. 5), during which the BIIS underwent several stages of advances and retreat (Peck et al., 2006, 2007; Peters et al., 2015, 2016). The BIIS reached its local maximum extent between 29 and 23 ka (Ó Cofaigh et al., 2012; Ó Cofaigh et al., 2021; Peters et al., 2015). At 27 ka BP, the BIIS advanced in all directions and was as far-reaching as the continental edge (Wilton et al., 2021). Consequently, it must be assumed that following the LGM, areas proximal to the BIIS, such as the wPB, experienced an amplified release of icebergs, ultimately increasing IRD deposition across the margin. Paleotidal modelling show that megatides influenced the Galway-Porcupine sector during early deglaciation (Scourse et al., 2018). This, in combination with a high rate of RSL rise and shallow water depth, may have been sufficient to further transport these icebergs from the north towards the wPB (Ward et al., 2020). The wPB would have acted as an obstacle for such southward flowing BIIS glaciers (Sacchetti et al., 2012), extensively scouring the area. Iceberg ploughmarks

identified in the north of the wPB core site (see Fig. 1 insert) are remnants of such icebergs, which ploughed the seabed during glacial sea level low stands (Dorschel et al., 2010). It is postulated that the erosive boundary identified in core CE118011_VC2 was caused by this intensive scouring. Sedimentation resumed following the retreat of the grounded ice on the seafloor, thought to be caused by glacio-isostatically induced high RSL (Ó Cofaigh et al., 2021). Indeed, the nearest modelled RSL for the wPB increases soon after the hiatus (Fig. 5e), supporting this hypothesis. However, as the wPB resides outside the maximum extent of the BIIS (e.g. Ó Cofaigh et al., 2012; Peters et al., 2015), the modelled RSL is greatly thus exaggerated, as this area of the margin did not experience isostatic rebound. Elsewhere, RSL from the Slyne Trough during the last glaciation show that sea levels decrease until 15 ka BP and deepen rapidly thereafter (Ó Cofaigh et al., 2021). As such, RSL estimations provided for the wPB should be interpreted with caution. Alternatively, the resumption of sedimentation could relate to the retreat of ice to land and/or could correlate with a thinner ice thickness. Either scenario would prevent further scouring of the wPB after 17.2 ka BP.

6. Conclusions

Using novel methods, this study documents the impact of BIIS glaciation on the wPB. ROV vibrocoring increased the accuracy of coring procedures and provided access to a once problematic study site. This method provides a forward for further paleoenvironmental coring missions, as it gives visual confirmation of sample acquisition and provides a brief survey of the sample site. Additionally, the analysis of non-destructive CT-scanning provided detailed sedimentological data every 0.02 cm. As such, this study is the highest resolution BIIS IRD record to date, which clearly describes each phase of IRD deposition in core CE18011_VC2 throughout the Late Pleistocene.

IRD fluxes are in part, concurrent with other NE Atlantic glacial reconstructions from 32.8 ka BP to 9 ka BP, which ultimately captures BIIS (de)glaciation. Using regional studies, this IRD material originated from glaciers that either a) followed the Malin Sea Ice Stream with minor input from the Irish Sea and Donegal Bay Ice Streams (Benetti et al., 2021; Purcell, 2018) or b) from an alternative route originating from the Galway-Porcupine Lobe. A detailed study on the composition of the IRD, would further clarify the provenance of this material. The wPB IRD record also suggests that an active calving margin were present in the region during the YD. Grain size distributions and mean sortable silt size illustrate that during glaciated events, bottom currents decelerate, which agrees with other studies from across the margin. A hiatus was identified from 27.3 to 17.2 ka BP and is the result of extensive iceberg scouring on the wPB.

Core CE18011_VC2 provides a useful analogue of IRD for areas proximal to the maximum extent of the BIIS. Additionally, results that demonstrate a reduced hydrodynamic regime during glacial events, would be well suited to a temporal assessment of nearby contemporaneous cold-water coral mounds, which likely experienced inhabitable conditions through the Late Pleistocene.

Data availability

CT dataset datasets related to this article can be found at https://github.com/lukeoreillyucc/CE18011_VC2, an open-source online data repository hosted at GitHub.com.

[dataset] Peck, Victoria L (2017): Paleoclimate records from core MD01-2461, PS, NE Atlantic. PANGAEA, https://doi.org/10.1594/PANGAEA.881905.

Author contributions

Luke O'Reilly: Investigation, Conceptualization, Formal analysis, Writing – original draft, Visualization, Data curation. Aaron Lim: Funding acquisition, Supervision, Investigation, Writing – review & editing. Jürgen Titschack: Methodology, Writing – review & editing. Niamh Moore: Methodology. OJ O'Connor: Methodology. John Appah: Investigation. Robin Fentimen: Writing – review & editing. Felix Butschek: Investigation, Writing – review & editing. Kimberley Harris: Project administration. Torsten Vennemann: Investigation, Writing – review & editing. Andrew Wheeler: Supervision, Funding acquisition, Writing – review & editing.

Declaration of competing interest

The authors declare that they have no known competing financial interests or personal relationships that could have appeared to influence the work reported in this paper.

Acknowledgements

The authors would like to thank Mr Paddy O′ Driscoll (P & O) for his assistance in developing the vibrocoring unit used in this study. We thank the JQS Editor Colm Ó Cofaigh for his patience and generosity with this extended contribution. The authors would like to express sincere thanks to James Scourse and an anonymous reviewer for their extremely helpful and thorough comments/suggestions on two earlier versions of the manuscript. All shiptime is funded under the National Development Plan (2019), National Grant-aided Shiptime Programme. Luke O'Reilly is funded by Science Foundation Ireland project "MMMonKey_Pro" ([grant number: 16/IA/4528]) which is co-funded by the Geological Survey Ireland and Marine Institute Ireland. Jürgen Titschack received funding from the Cluster of Excellence "The Ocean Floor—Earth's Uncharted Interface" (Germany's Excellence Strategy—EXC-2077-390741603 of the DFG). Felix Butschek is funded from the European Union's Horizon 2020 research and innovation program under grant agreement No 818123 (iAtlantic). The authors would like to thank the MMMonKey_Pro team members and members of the Marine Geosciences Research Group at UCC, as well as scientific parties, officers, and crew of cruise CE18011. All authors have read and approved the manuscript.

Appendices

Appendix A. Computed Tomography Processing Procedures

The raw DICOM data were processed with the ZIB edition of Amira software (version 2018.36; Stalling et al., 2005; http://amira.zib.de). Within Amira, the CT scans of the cores liners, including approx. 2 mm of the core rims, were removed from the data set (using a combination of the segmentation editor and the *Arithmetic* tool) to remove density artefacts resulting from the coring process. Isotropic voxels were generated by reducing each voxel size to 0.2 mm in all dimensions, correcting for partial volume averaging errors. An isosurface was created to visualise the dataset in 3D space, which was then re-positioned interactively through the live module in the software, to account for any offsets during scanning. The resampled dataset was reformatted using the Lanczos interpolation method, which tries to approximate a low-pass filter that is in accordance with the sampling theorem, thus sharpening images (see *Amira Reference Guide*, *Visage Imaging*). The macroscopic sediment components (>*ca* 1 mm), dominated by IRD, were quantified in each CT-slice with the segmentation editor (Threshold value: 1400) and the *MaterialStatistics* module (volume per slice) to

understand IRD deposition phases. Further evaluation of these components was performed with the *ContourTreeSegmentation* algorithm (Threshold: 1400; Persistence Value: 1100) which is based on the concept of contour trees and functions similar to hieratical watershed segmentation and topological persistence (see (Titschack et al., 2015) and references therein). This created an automatic segmentation of the 3D macroscopic components. At this stage, the IRD CT results were visually checked to asses if the 3D segmentation was correctly applied. The *ShapeAnalysis* module and *GrainSizeDistribution* module were used to characterise each component. Clast length [unit: $\phi = \log_2$ [length (mm)/1 mm]] was used to analyse clast size. Therefore, every clast within a window of 51 CT-slices (about 1 cm) was counted and the result was added to a spreadsheet. The analysing window was moved slice by slice. Moreover, the *ShapeAnalysis* module and *GrainAngleDistribution* module were used to characterise the z-orientation of the major axis of each clast in a similar manner, whereby horizontal = 0° and vertical = 90°. Additionally, X-ray density of the matrix sediment was determined by calculating the mean value and its standard deviation of the matrix sediment per slice. The final results were exported to a spreadsheet. IRD patterns were analysed using exported results from Amira (vol. % and clasts per cm^{-3}).

Appendix B. Organic Matter and Carbonate Dissolution Procedures

Subsamples of roughly 1 cm^3 of sediment were taken from the core at 5 cm intervals. Each sample was assigned to a pre-weighed beaker, and oven-dried at 60 °C for 24 h. When dry, the sample was left cool for 30 min. At this stage, any large bioclasts (>2 mm) which may have been extracted in the initial sampling stage were removed. 200 ml of distilled water and 10 ml of 10% HCl were added to each beaker and heated to 90 °C for 2 h to dissolve the carbonate fraction of the sample. If an incomplete reaction occurred, extra heat and HCl were added. The samples were given 1 h to settle. Any remaining solution was removed with a syringe, taking care not to disturb any sediment on the bottom of the beaker. The samples were then oven dried at 60 °C for 24 h. Once dry, the sample was left cool for a further 30 min and weighed. The aforementioned steps were repeated, using a solution of 10 ml of 10% H_2O_2 to oxidise organic matter from the samples. When complete, the samples were dried at 60 °C for 24 h. When completely dry the sample was left cool again for a further 30 min and weighed again. This final weight represents the total lithic component of the sample. Each sample was sieved through a 2 mm sieve, removing larger lithoclasts from the sample. These clasts were weighed and stored in individual containers. The sieved samples were stored in individual test tubes with 30 ml of distilled water and a solution of 5.5 g/l sodium tetraphosphate for at least 24 h. This chemical dispersant prevented grains from aggregating during the grain-size measurements as well as after sonication.

Appendix C. Grain Size Analysis and Operating Procedures

Prior to analysis, method building was required to ensure the best representative results were retrieved with the MS3000 by optimising the machine parameters. Variations on obscuration %, stirrer speed and ultrasonic duration were determined using a fine and coarse sediment fraction, insuring a representative control on the experiment. When a consistent relative standard deviation (RSD) value < 2% was yielded, these parameters constructed standard operating procedures for the study (see table below). All samples showed stability using these methods. The measurement procedure in the MS3000 was carried out with deionized water. Prior to adding the sample to the MS3000 wet dispersion unit, the sample was shaken by hand for approximately 10 s to minimize flocculation of particles. The sample was then introduced into the wet dispersion unit using a 1 ml pipette, allowing the addition to occur in a controlled manner. Before accepting a grain size value, the data was first inspected for anomalous results which could be attributed to air bubbles or operational errors.

PSA Operating Procedures		
Particle Type		
Non-spherical		
Material Properties		
Quartz		
Refractive Index: 1.543	*Absorption Index: 0.01*	*Density (g/cm³): 1*
Dispersant Properties		
Water		
Refractive Index: 1.33	*Level Sensor threshold: 75*	
Measurement Duration (seconds)		
Red		
Background: 10	*Sample: 10*	
Blue		
Background: 10	*Sample: 10*	
Number of measurements		
5		
Clean Type		
Normal (3 clean cycles)		
Analysis settings		
General purpose		
Stirrer Speed (rmp)		
Fine: 2400	Coarse: up to 3400	
Obscuration%		
Fine: 10–15%	Coarse: 15–20%	
Ultrasonication (seconds)		
Fine: 120	Coarse: up to 240	

Appendix D. End-member modelling

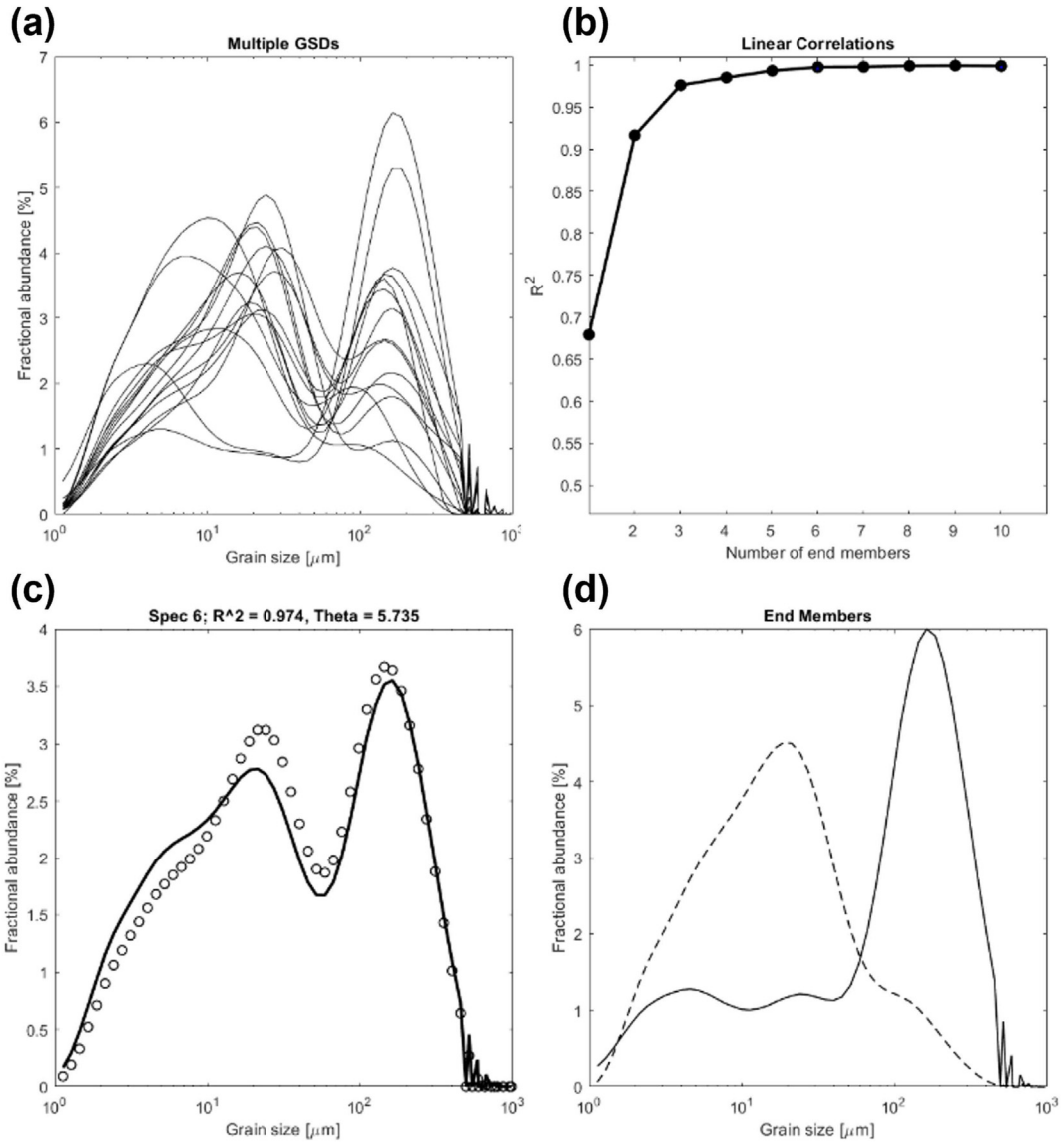

Goodness-of-fit statistics applied to estimate the number of end members. (a) all of the grain-size distributions used in the model; (b) r^2 values for CE18011_VC2 end-member models with 2–10 end members. With 2 end members a value of $r^2 = 0.92$ is acquired; (c) The application of the two end member model to grain size data from 30 cmbsf. Modelled (black) vs measured (circles); (d) Unmixed contributions of the model displaying EMa (dashed line) and EMb (black line).

Appendix E. Correlation of sortable silt (%) versus mean sortable silt (μm)

Two outliers were removed from this analysis (red boxes), which significantly increased the correlation coefficient by 0.5.

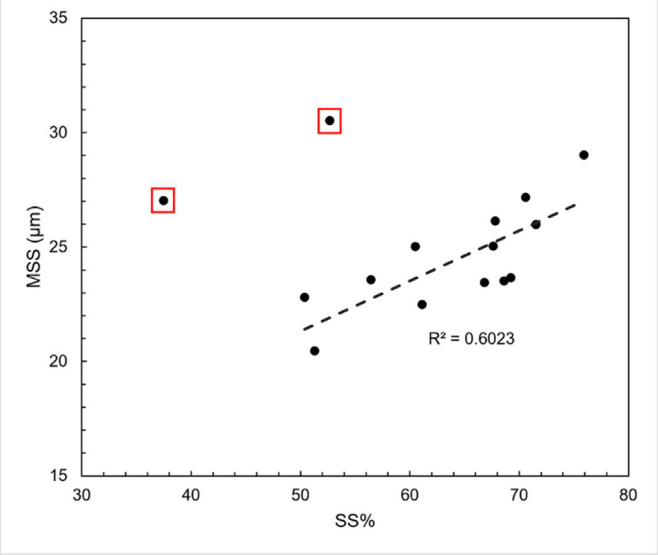

Appendix F. Age model parameters

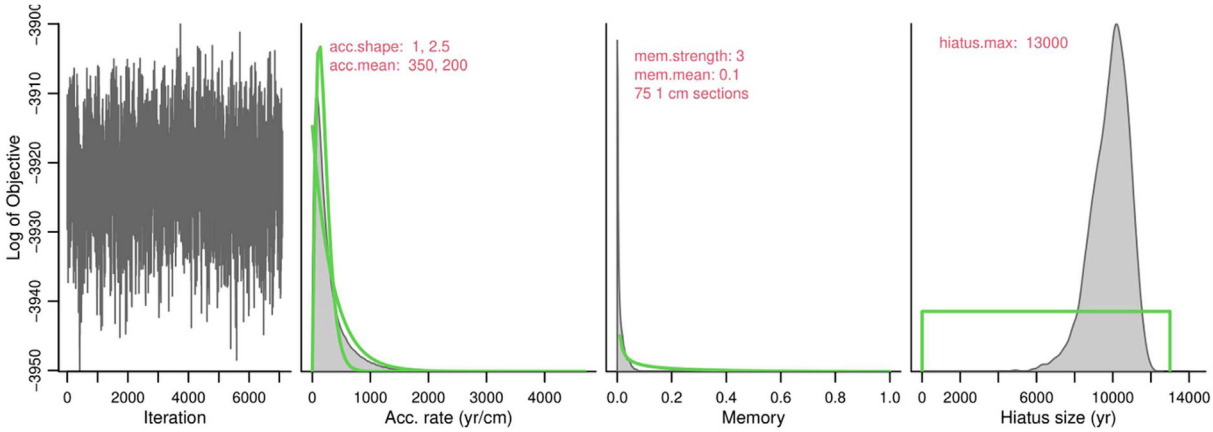

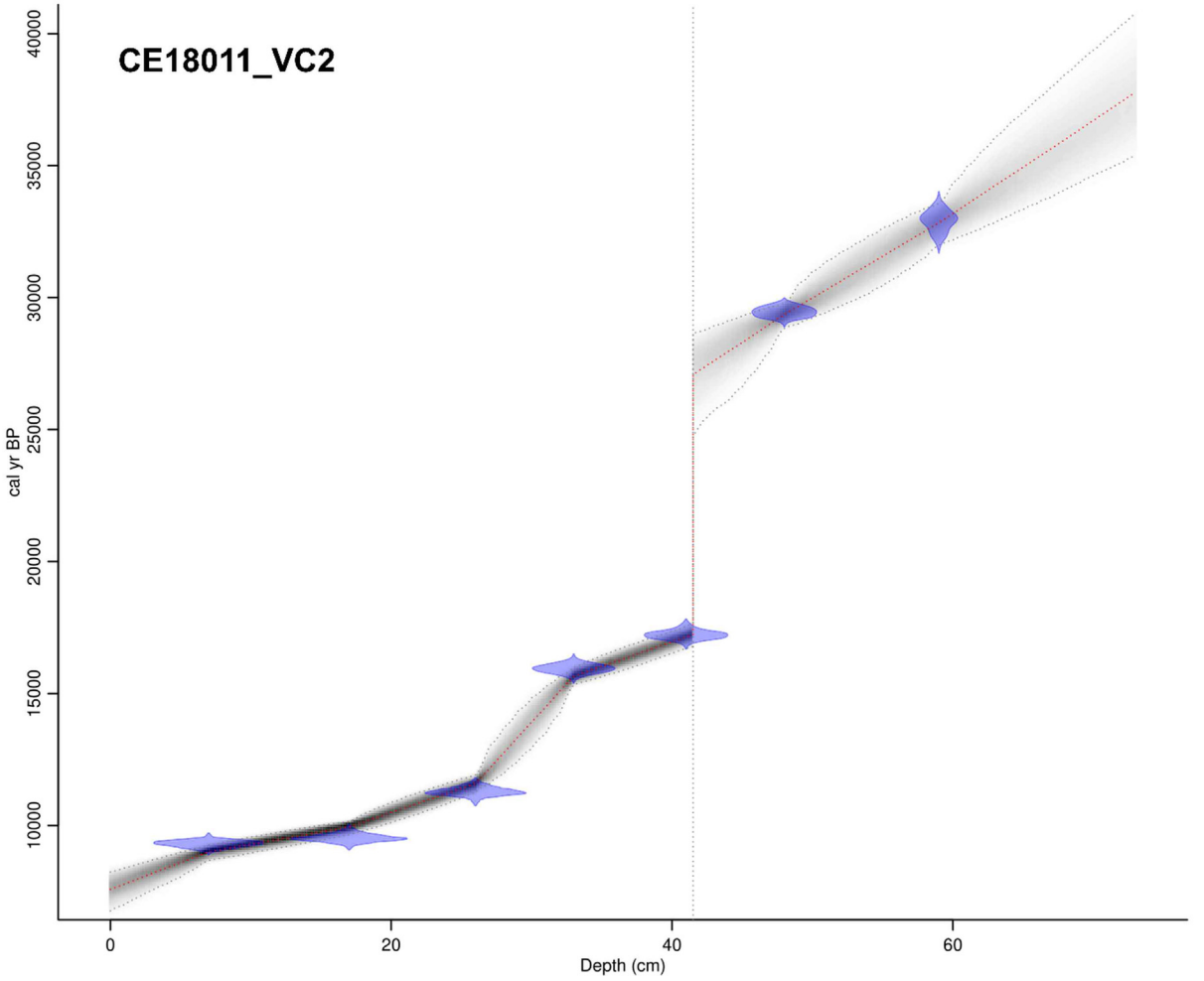

Appendix G. Additional Sedimentological Data Plot

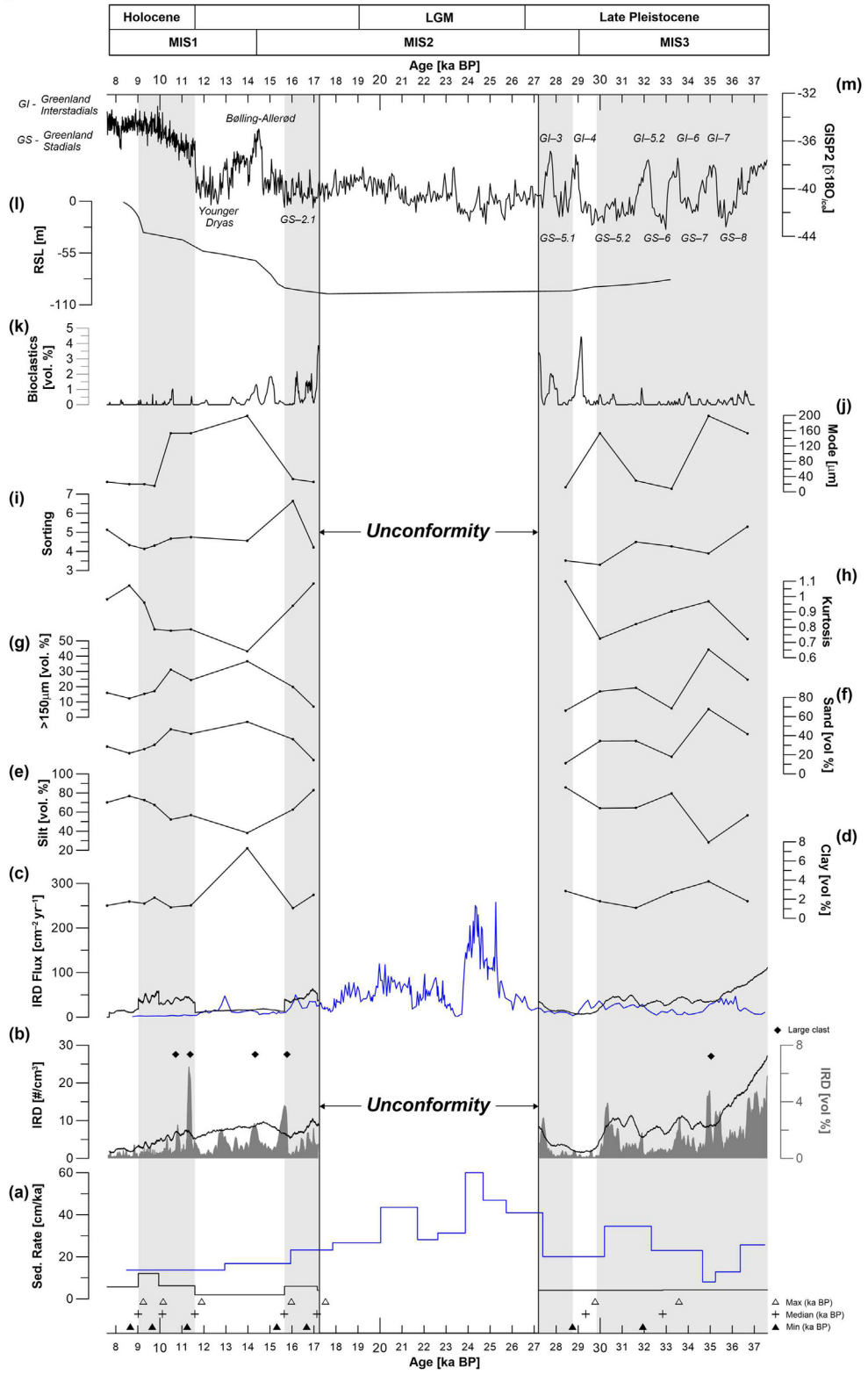

Continuation of additional multi-proxy data obtained from core VC18011_VC2 excluded from Fig. 5. Compilation of multi-proxy data obtained from core VC18011_VC2 (in black and grey) plotted against time compared to the data of Peck et al., (2006) from the Porcupine Seabight (in blue). Includes an unconformity from 27.3 to 17.2 ka BP. Periods containing high IRD fluxes are shown as shaded grey areas. Modelled ages (in kiloyears BP) at bottom are annotated by black cross (median), white triangles (maximum) and black triangles (minimum) (a) sedimentation rates; (b) IRD volume percentage (solid black line), IRD clasts per cubic centimetre (light grey filled in); (c) IRD flux (d–f) volume percentage derived from grain size analysis of clay, silt and sand (g) Volume percentage of grains >150 μm; (h) kurtosis (higher kurtosis indicate more peaked profiles; (i) sorting of grain size distributions. An increase in this proxy indicates sediments become less sorted (j) size of mode 1 of grain size distributions (k) volume percentage of biogenic clasts derived from CT-data; (l) Relative sea-level estimates in metres were calculated from models composed by (Brooks et al., 2008) and was simulated by the glacial rebound model of Bradley (2011) and applied to the area (personal communication Robin Edwards, Trinity College Dublin, 2021); (m) GISP Greenland Ice Core δ18O values.

Appendix H. Tables

Appendix H.1: Sedimentological data for core CE18011_VC2

Depth [cmbsf]	Sand [vol%]	Silt [vol%]	Clay [vol%]	>150 μm [vol%]	$CaCO_3$ Cont. [wt.%]	MGS [μm]	MSS [μm]	Sorting [μm]	Kurtosis	Settling Velocity [ms^{-1}]
0	28.6	70.1	1.3	16.0	40.6	30.1	26.0	4.3	0.98	0.37
5	21.6	76.7	1.8	12.4	45.7	23.1	23.5	4.1	1.07	0.30
10	26.0	72.5	1.5	15.3	47.0	26.9	23.5	4.3	0.96	0.30
15	30.3	67.5	2.2	17.2	51.2	25.8	22.5	4.7	0.79	0.28
20	46.7	52.2	1.2	31.2	51.2	46.0	23.7	4.8	0.78	0.31
25	42.0	56.7	1.3	24.4	39.0	38.0	26.1	4.6	0.78	0.37
30	54.4	38.2	7.3	36.7	26.6	42.2	27.0	6.6	0.64	0.40
35	36.2	62.7	1.1	19.9	46.6	38.5	29.0	4.2	0.94	0.46
40	14.5	83.1	2.5	7.0	30.9	17.7	25.0	3.5	1.09	0.34
45	11.2	85.9	2.9	4.4	12.5	12.0	20.5	3.3	1.10	0.23
50	34.3	63.9	1.8	16.9	31.0	27.5	25.0	4.5	0.72	0.34
55	34.5	64.5	1.1	19.3	43.0	33.8	27.2	4.3	0.82	0.40
60	17.8	79.5	2.7	5.8	24.8	15.2	22.8	3.9	0.90	0.29
65	67.8	28.4	3.9	44.4	27.1	64.2	30.4	5.3	0.97	0.51
70	41.7	56.5	1.8	24.7	29.1	32.7	23.6	5.1	0.72	0.30

References

Andresen, C.S., McCarthy, D.J., Dylmer, C.V., Seidenkrantz, M.-S., Kuijpers, A., Lloyd, J.M., 2011. Interaction between subsurface ocean waters and calving of the Jakobshavn Isbrae during the late Holocene. Holocene 21, 211–224. https://doi.org/10.1177/0959683610378877.

Andrews, J., 2000. Icebergs and iceberg rafted detritus (IRD) in the North Atlantic: facts and assumptions. Oceanography 13, 100–108. https://doi.org/10.5670/oceanog.2000.19.

Appah, J.K.M., Lim, A., Harris, K., O'Riordan, R., O'Reilly, L., Wheeler, A.J., 2020. Are non-reef habitats as important to benthic diversity and composition as coral reef and rubble habitats in submarine canyons? Analysis of controls on benthic megafauna distribution in the Porcupine Bank canyon, NE atlantic. Front. Mar. Sci. 7. https://doi.org/10.3389/fmars.2020.571820.

Arosio, R., Crocket, K.C., Nowell, G.M., Callard, S.L., Howe, J.A., Benetti, S., Fabel, D., Moreton, S.G., Clark, C.D., 2017. Weathering fluxes and sediment provenance on the SW Scottish shelf during the last deglaciation. Mar. Geol. 402, 81–98. https://doi.org/10.1016/j.margeo.2017.08.017.

Austin, W., Telford, R., Ninnemann, U., Brown, L., Wilson, L., Small, D., Bryant, C., 2011. North Atlantic reservoir ages linked to high Younger Dryas atmospheric radiocarbon concentrations. Global Planet. Change 79, 226–233. https://doi.org/10.1016/j.gloplacha.2011.06.011.

Ballantyne, C., Ó Cofaigh, C., 2017. The last Irish ice sheet: extent and chronology. Adv. Irish Quatern. Stud. https://doi.org/10.2991/978-94-6239-219-9_5.

Bartels, M., Titschack, J., Fahl, K., Stein, R., Hebbeln, D., 2018. Wahlenbergfjord, eastern Svalbard: a glacier surrounded fjord reflecting regional hydrographic variability during the Holocene? Boreas 47, 1003–1021. https://doi.org/10.1111/bor.12325.

Bartels, M., Titschack, J., Fahl, K., Stein, R., Seidenkrantz, M.-S., Hillaire-Marcel, C., Hebbeln, D., 2017. Atlantic Water advection vs. glacier dynamics in northern Spitsbergen since early deglaciation. Clim. Past 13, 1717–1749. https://doi.org/10.5194/cp-13-1717-2017.

Bateman, M.D., Evans, D.J.A., Roberts, D.H., Medialdea, A., Ely, J.C., Clark, C.D., 2017. The timing and consequences of the blockage of the Humber Gap by the last British Irish Ice Sheet. Boreas 47, 41–61. https://doi.org/10.1111/bor.12256.

Benetti, S., Chiverrell, R.C., Ó Cofaigh, C., Burke, M.J., Medialdea, A., Small, D.L., Ballantyne, C.K., Bateman, M.D., Callard, S.L., Wilson, P., Fabel, D., Clark, C.D., Arosio, R., Bradley, S.L., Dunlop, P., Ely, J.C., Gales, J., Livingstone, S.J., Moreton, S.G., Purcell, C., Saher, M., Schiele, K., Van Landeghem, K.J.J., Weilbach, K., 2021. Exploring controls of the early and stepped deglaciation on the western margin of the British Irish Ice Sheet. J. Quat. Sci. 36, 388–870. https://doi.org/10.1002/jqs.3315.

Bigg, G.R., Clark, C., Greenwood, S., Haflidason, H., Hughes, A., Levine, R., Nygård, A., Sejrup, H.P., 2012. Sensitivity of the North Atlantic circulation to break-up of the marine sectors of the NW European ice sheets during the last Glacial: a synthesis of modelling and palaeoceanography. Global Planet. Change 98, 153–165. https://doi.org/10.1016/j.gloplacha.2012.09.004.

Blaauw, M., Christen, J.A., 2011. Flexible paleoclimate age-depth models using an autoregressive gamma process. Bayesian Anal. 6, 457–474. https://doi.org/10.1214/ba/1339616472.

Blaauw, M., Christen, J.A., Aquino, A., 2020. Age-Depth Modelling Using Bayesian Statistics [R Package Rbacon, version 2.5.0.

Black, K.S., Peppe, O.C., Gust, G., 2003. Erodibility of pelagic carbonate ooze in the Northeast Atlantic. J. Exp. Mar. Biol. Ecol. 285, 143–163. https://doi.org/10.1016/S0022-0981(02)00524-5.

Blott, S.J., Pye, K., 2001. GRADISTAT: a grain size distribution and statistics package for the analyses of unconsolidated sediments. Earth Surf. Process. Landforms 26, 1237–1248. https://doi.org/10.1002/esp.261.

Bond, G.C., Broecker, W.S., Johnsen, S.J., McManus, J.F., Labeyrie, L., Jouzel, J., Bonani, G.G., 1993. Correlations between climate records from North Atlantic sediments and Greenland ice. Nature 365, 143–147. https://doi.org/10.1038/365143a0.

Boulton, G., 1996. The origin of till sequences by subglacial sediment deformation beneath mid-latitude ice sheets. Ann. Glaciol. 22, 75–84. https://doi.org/10.1017/S026030550001524X.

Bradley, S., 2011. Using sea-level and land motion data to develop an improved glacial isostatic adjustment model for the British Isles. J. Quat. Sci. 26, 541–552. https://doi.org/10.1002/jqs.1481.

Bradwell, T., Small, D.L., Fabel, D., Smedley, R.K., Clark, C.D., Saher, M.H., Callard, S.L., Chiverrell, R.C., Dove, D., Moreton, S.G., Roberts, D.H., Duller, G.A.T., Ó Cofaigh, C., 2019. Ice-stream demise dynamically conditioned by trough shape and bed strength. Sci. Adv. 5. https://doi.org/10.1126/sciadv.aau1380.

Brooks, A., Bradley, S., Edwards, R., Milne, G., Horton, B., Shennan, I., 2008. Post-glacial relative sea level observations from Ireland and their role in glacial rebound modelling. J. Quat. Sci. 23, 821–825. https://doi.org/10.1002/jqs.1119.

Callard, S., Ó Cofaigh, C., Benetti, S., Chiverrell, R., Landeghem, K.V., Saher, M.H., Gales, J., Small, D., Clark, C., Stephen, J.L., Fabel, D., Moreton, S.G., 2018. Extent and retreat history of the Barra Fan Ice Stream offshore western Scotland and northern Ireland during the last glaciation. Quat. Sci. Rev. 201, 280–302. https://doi.org/10.1016/j.quascirev.2018.10.002.

Callard, S.L., Ó Cofaigh, C., Benetti, S., Chiverrell, R., Landeghem, K.V., Saher, M., Livingstone, S., Clark, C., Small, D., Fabel, D., Moreton, S., 2020. Oscillating retreat of the last British-Irish Ice Sheet on the continental shelf offshore Galway Bay, western Ireland. Mar. Geol. 420, 106087. https://doi.org/10.1016/j.margeo.2019.106087.

Carr, J.R., Vieli, A., Stokes, C.R., 2013. Influence of sea ice decline, atmospheric warming, and glacier width on marine-terminating outlet glacier behavior in northwest Greenland at seasonal to interannual timescales. J. Geophys. Res. 118, 1210–1226. https://doi.org/10.1002/jgrf.20088.

Chiverrell, R.C., Smedley, R.K., Small, D.L., Ballantyne, C.K., Burke, M.J., Callard, S.L., Clark, C.D., Duller, G.A.T., Evans, D.J.A., Fabel, D., Landeghem, K.J.J.V., Livingstone, S.J., Ó Cofaigh, C., Thomas, G.S.P., Roberts, D.H., Saher, M.H., Scourse, J.D., Wilson, P., 2018. Ice margin oscillations during deglaciation of the northern Irish Sea basin. J. Quat. Sci. 33, 739–762. https://doi.org/10.1002/jqs.3057.

Clark, P.U., Dyke, A.S., Shakun, J.D., Carlson, A.E., Clark, J., Wohlfarth, B., Mitrovica, J.X., Hostetler, S.W., Mccabe, A., 2009. The last glacial maximum. Science 325, 710–714. https://doi.org/10.1126/science.1172873.

Clark, C., Hughes, A., Greenwood, S., Jordan, C., Sejrup, H.P., 2012. Pattern and timing of retreat of the last British-Irish Ice Sheet. Quat. Sci. Rev. 44, 112–146. https://doi.org/10.1016/j.quascirev.2010.07.019.

Cowan, E., Hillenbrand, C., Hassler, L., Ake, M.T., 2008. Coarse-grained terrigenous sediment deposition on continental rise drifts: a record of Plio-Pleistocene glaciation on the Antarctic Peninsula. Palaeogeogr. Palaeoclimatol. Palaeoecol. 265, 275–291. https://doi.org/10.1016/j.palaeo.2008.03.010.

Damiani, D., Giorgetti, G., Turbanti, I., 2006. Clay mineral fluctuations and surface textural analysis of quartz grains in Pliocene Quaternary marine sediments from Wilkes Land continental rise (East-Antarctica): paleoenvironmental significance. Mar. Geol. 226, 281–295. https://doi.org/10.1016/j.margeo.2005.11.002.

deGelleke, L., Hill, P., Kienast, M., Piper, D.J., 2013. Sediment dynamics during Heinrich event H1 inferred from grain size. Mar. Geol. 336, 160–169. https://doi.org/10.1016/j.margeo.2012.12.007.

Dickson, R.R., McCave, I.N., 1986. Nephloid layer on the continental slope west of Porcupine Bank. Deep Sea Res. 33, 791–818. https://doi.org/10.1016/0198-0149(86)90089-0.

Dorschel, B., Hebbeln, D., Rüggeberg, A., Dullo, W.-C., Freiwald, A., 2005. Growth and erosion of a cold-water coral covered carbonate mound in the Northeast Atlantic during the late Pleistocene and Holocene. Earth Planet Sci. Lett. 233, 33–44. https://doi.org/10.1016/j.epsl.2005.01.035.

Dorschel, B., Wheeler, A.J., Monteys, X., Verbruggen, K., 2010. Atlas of the Deep-Water Seabed: Ireland. Springer, Dordrecht Heidelberg London New York. https://doi.org/10.1007/978-90-481-9376-1.

Eldrett, J., Harding, I., Wilson, P., Butler, E., Roberts, A.P., 2007. Continental ice in Greenland during the eocene and Oligocene. Nature 446, 176–179. https://doi.org/10.1038/nature05591.

Elliott, G.M., Shannon, P.M., Haughton, P.D.W., Praeg, D., O'Reilly, B., 2006. Mid- to Late Cenozoic canyon development on the eastern margin of the Rockall Trough, offshore Ireland. Mar. Geol. 229, 113–132. https://doi.org/10.1016/j.margeo.2006.03.008.

Evans, D.J.A., Bateman, M.D., Roberts, D.H., Medialdea, A., Hayes, L., Duller, G.A.T., Fabel, D., Clark, C.D., 2017. Glacial lake pickering: stratigraphy and chronology of a proglacial lake dammed by the north sea Lobe of the British Irish ice sheet. J. Quat. Sci. 32, 295–310. https://doi.org/10.1016/j.margeo.2006.03.008.

Evans, D.J.A., Roberts, D.H., Bateman, M.D., Ely, J.C., Medialdea, A., Burke, M.J., Chiverrell, R.C., Clark, C.D., Fabel, D., 2019. A chronology for north sea Lobe advance and recession on the lincolnshire and norfolk coasts during MIS 2 and 6. Proc. Geologists' Assoc. https://doi.org/10.1016/j.pgeola.2018.10.004.

Evans, D.J.A., Roberts, D.H., Bateman, M.D., Medialdea, A., Ely, J.C., Moreton, S.G., Clark, C.D., Fabel, D., 2018. Sedimentation during MIS 3 at the eastern margins of the glacial lake humber basin, england. J. Quat. Sci. 33, 871–891. https://doi.org/10.1002/jqs.3066.

Folk, R.L., Ward, W., 1957. Brazos River bar [Texas]; a study in the significance of grain size parameters. J. Sediment. Res. 27, 3–26. https://doi.org/10.1306/74D70646-2B21-11D7-8648000102C1865D.

Georgiopoulou, A., Benetti, S., Shannon, P.M., Haughton, P.D., McCarron, S., 2012. Gravity Flow Deposits in the Deep Rockall Trough, Northeast Atlantic, Submarine Mass Movements and Their Consequences. Springer, pp. 695–707. https://doi.org/10.1007/978-94-007-2162-3_62.

Greenwood, S., Clark, C., 2009. Reconstructing the last Irish Ice Sheet 1 : changing flow geometries and ice flow dynamics deciphered from the glacial landform record. Quat. Sci. Rev. 28, 3085–3100. https://doi.org/10.1016/j.quascirev.2009.09.008.

Hall, I., McCave, I.N., 1998a. Glacial-interglacial variation in organic carbon burial on the slope of the N.W. European Continental Margin (48° 50°N). Prog. Oceanogr. 42, 37–60. https://doi.org/10.1016/S0079-6611(98)00027-5.

Hall, I., McCave, I.N., 1998b. Late Glacial to Recent accumulation fluxes of sediments at the shelf edge and slope of NW Europe, 48-50°N. Geol. Soc. Lond. Sp. Publ. 129, 339–350. https://doi.org/10.1144/GSL.SP.1998.129.01.20.

Hateren, J.A.V., Prins, M., Balen, R.V., 2017. On the genetically meaningful decomposition of grain-size distributions: a comparison of different end-member modelling algorithms. Sediment. Geol. 375, 49–71. https://doi.org/10.1016/j.sedgeo.2017.12.003.

Heaton, T.J., Koehler, P., Butzin, M., Bard, É., Reimer, R., Austin, W., Ramsey, C., Grootes, P., Hughen, K., Kromer, B., Reimer, P.J., Adkins, J., Burke, A., Cook, M., Olsen, J.V., Skinner, L., 2020. Marine20 the marine radiocarbon age calibration curve (0 55,000 cal BP). Radiocarbon 62, 779–820. https://doi.org/10.1017/RDC.2020.68.

Heinrich, H., 1988. Origin and consequences of cyclic ice rafting in the northeast

atlantic ocean during the past 130,000 years. Quat. Res. 29, 142–152. https://doi.org/10.1016/0033-5894(88)90057-9.
Helland, P.E., Holmes, M., 1997. Surface textural analysis of quartz sand grains from ODP Site 918 off the southeast coast of Greenland suggests glaciation of southern Greenland at 11 Ma. Palaeogeogr. Palaeoclimatol. Palaeoecol. 135, 109–121. https://doi.org/10.1016/S0031-0182(97)00025-4.
Jacobs, W., Hir, P.L., Kesteren, W.G.M.v., Cann, P., 2011. Erosion threshold of san,, mud mixtures. Continent. Shelf Res. 31, S15–S25. https://doi.org/10.1016/j.csr.2010.05.012.
Jones, C., Lawton, J., Shachak, M., 1994. Organisms as ecosystem engineers. Oikos 69, 130–147. https://doi.org/10.1007/978-1-4612-4018-1_14.
Jonkers, L., Barker, S., Hall, I., Prins, M., 2015. Correcting for the influence of ice rafted detritus on grain size based paleocurrent speed estimates. Paleoceanography 30, 1347–1357. https://doi.org/10.1002/2015PA002830.
Knutz, P.C., Austin, W.E.N., Jones, E.J.W., 2001. Millennial-scale depositional cycles related to British ice sheet variability and North Atlantic paleocirculation since 48 kyr B.P., barra fan, U.K. margin. Paleoceanography 16, 53–64. https://doi.org/10.1029/1999PA000483.
Kuijpers, A., Knutz, P., Moros, M., 2013. Ice-rafted debris (IRD). In: Harff, J., Meschede, M., Petersen, S., Thiede, J. (Eds.), Encyclopedia of Marine Geosciences. Springer Netherlands, Dordrecht, pp. 1–7. https://doi.org/10.1007/978-94-007-6238-1_182.
Lim, A., O' Reilly, L., Burke, S., Wheeler, A., Appah, J., Summers, G., Harris, K., Shine, A., Boolukos, C., McAleer, A., Conti, L., Holland 1 ROV technical team, Officers and Crew of the RV Celtic Explorer, 2018. Controls of Cold-Water Coral Habitats in Submarine Canyons, Survey (CoCoHaCa II) of the Porcupine Bank Canyon, Cruise Report. https://www.ucc.ie/en/media/research/marinegeo/mgpdfs/Cruise-Report-CoCoHaCa-II.pdf.
Lim, A., Wheeler, A.J., Price, D., O'Reilly, L., Harris, K., Conti, L., 2020. Influence of benthic currents on cold-water coral habitats: a combined benthic monitoring and 3D photogrammetric investigation. Sci. Rep. 10. https://doi.org/10.1038/s41598-020-76446-y.
Lim, A.O.R., Luke, Summers, Gerard, Harris, Kim, Macedo, Larissa, O' Hanlon, Zoe, Appah, John, O' Mahony, Evan, Strachan, Ruaihri, Walsh, Phoebe, Wheeler, Andy, 2019a. CE19014 cruise report: monitoring changes in submarine canyon coral habitats - leg 2 (MoCha_Scan II). https://www.ucc.ie/en/media/research/marinegeo/mgpdfs/MoCha_SCan_II_Cruise_Report-1.pdf.
Lim, A.O.R., Luke, Summers, Gerard, Harris, Kim, Shine, Andrew, Harman, Luke, Macedo, Larissa, Boyd, John, Anders, Bebhinn, Killeen, Orla, Conti, Luis, O' Brien, Martina, Holland 1 ROV technical team, Officers and Crew of the RV Celtic Explorer, 2019b. CE19008 cruise report: monitoring changes in submarine canyon coral habitats - leg 1 (MoCha_SCan), cruise report. https://www.ucc.ie/en/media/research/marinegeo/mgpdfs/MoCha_SCan_Cruise_Report0.pdf.
Lloyd, J.M., Moros, M., Perner, K., Telford, R.J., Kuijpers, A., Jansen, E., McCarthy, D.J., 2011. A 100 yr record of ocean temperature control on the stability of Jakobshavn Isbrae, West Greenland. Geology 39, 867–870. https://doi.org/10.1130/G32076.1.
Lockhart, E., Scourse, J.D., Praeg, D., Landeghem, K.J.J.V., Mellett, C.L., Saher, M.H., Callard, L., Chiverrell, R.C., Benetti, S., Ó Cofaigh, C., Clark, C.D., 2018. A stratigraphic investigation of the Celtic Sea megaridges based on seismic and core data from the Irish-UK sectors. Quat. Sci. Rev. 198, 156–170. https://doi.org/10.1016/j.quascirev.2018.08.029.
Mahaney, W., 2002. Atlas of Sand Grain Surface Textures and Applications. Oxford Univiversity Press, New York.
Mahaney, W., Kalm, V., 2000. Comparative scanning electron microscopy study of oriented till blocks, glacial grains and Devonian sands in Estonia and Latvia. Boreas 29, 35–51. https://doi.org/10.1111/j.1502-3885.2000.tb01199.x.
Manighetti, B., McCave, I.N., 1995a. Depositional fluxes, palaeoproductivity, and ice rafting in the NE Atlantic over the past 30 ka. Paleoceanography 10, 579–592. https://doi.org/10.1029/94PA03057.
Manighetti, B., McCave, I.N., 1995b. Late glacial and Holocene palaeocurrents around Rockall bank, NE atlantic ocean. Paleoceanography 10, 611–626. https://doi.org/10.1029/94PA03059.
Mazzini, A., Akhmetzhanov, A., Monteys, X., Ivanov, M., 2011. The Porcupine Bank Canyon coral mounds: oceanographic and topographic steering of deep-water carbonate mound development and associated phosphatic deposition. Geo Mar. Lett. 32, 205–225. https://doi.org/10.1007/s00367-011-0257-8.
McCabe, A., Clark, P., 1998. Ice-sheet variability around the North Atlantic Ocean during the last deglaciation. Nature 392, 373–377. https://doi.org/10.1038/32866.
McCave, I.N., Andrews, J., 2019. Distinguishing current effects in sediments delivered to the ocean by ice. I. Principles, methods and examples. Quat. Sci. Rev. 212, 92–107. https://doi.org/10.1016/j.quascirev.2019.03.031.
Mccave, I.N., Andrews, J., 2019. Distinguishing current effects in sediments delivered to the ocean by ice. II. Glacial to Holocene changes in high latitude North Atlantic upper ocean flows. Quat. Sci. Rev. 223, 105902. https://doi.org/10.1016/j.quascirev.2019.105902.
McCave, I.N., Manighetti, B., Beveridge, N.A.S., 1995a. Circulation in the glacial North Atlantic inferred from grain-size measurements. Nature 374, 149–152. https://doi.org/10.1038/374149a0.
McCave, I.N., Manighetti, B., Robinson, S.G., 1995b. Sortable silt and fine sediments size/composition slicing: parameters for paleocurrent speed and palaeoceanography. Paleoceanography 10, 593–610. https://doi.org/10.1029/94PA03039.
McLaren, P.L., 1981. An interpretation of trends in grain size measures. J. Sediment. Res. 51, 611–624. https://doi.org/10.1306/212F7CF2-2B24-11D7-8648000102C1865D.
Naylor, D., Shannon, P., 1975. Geology of Offshore Ireland and West Britain. https://doi.org/10.1007/978-94-010-9358-3.
Ó Cofaigh, C., Dunlop, P., Benetti, S., 2012. Marine geophysical evidence for Late Pleistocene ice sheet extent and recession off northwest Ireland. Quat. Sci. Rev. 44, 147–159. https://doi.org/10.1016/j.quascirev.2010.02.005.
Ó Cofaigh, C., Weilbach, K., Lloyd, J., Benetti, S., Callard, S., Purcell, C., Chiverrell, R., Dunlop, P., Saher, M.H., Livingstone, S., Landeghem, K.V., Moreton, S.G., Clark, C., Fabel, D., 2019. Early deglaciation of the British-Irish Ice Sheet on the Atlantic shelf northwest of Ireland driven by glacioisostatic depression and high relative sea level. Quat. Sci. Rev. 208, 76–96. https://doi.org/10.1016/j.quascirev.2018.12.022.
Ó Cofaigh, C., Callard, S.L., Roberts, D.H., Chiverrell, R.C., Ballantyne, C.K., Evans, D.J.A., Saher, M., Van Landeghem, K.J.J., Smedley, R.K., Benetti, S., Burke, M.J., Clark, C.D., Duller, G.A.T., Fabel, D., Livingstone, S.J., Mccarron, S., Medialdea, A., Moreton, S.G., Sacchetti, F., 2021. Timing and pace of ice-sheet withdrawal across the marine–terrestrial transition west of Ireland during the last glaciation. J. Quat. Sci. 36, 805–832. https://doi.org/10.1002/jqs.3295.
Øvrebø, L.K., Haughton, P.D.W., Shannon, P.M., 2006. A record of fluctuating bottom currents on the slopes west of the Porcupine Bank, offshore Ireland; implications for late Quaternary climate forcing. Mar. Geol. 225, 279–309. https://doi.org/10.1016/j.margeo.2005.06.034.
Øvrebø, L.K., Shannon, P., 2005. Temporal and spatial variations in Late Quaternary slope sedimentation along the undersupplied margins of the Rockall Trough, offshore west Ireland. Norw. J. Geol. 85, 279–294.
Owen, N., 2010. A Multi-Proxy Palaeoceanographic Investigation of Slope Deposits on Porcupine Bank, NE Atlantic Ocean. Thesis. Trinity College (Dublin, Ireland). Department of Geology. Doctor of Philosophy (Ph.D.). http://hdl.handle.net/2262/78164.
Paterson, G., Heslop, D., 2015. New methods for unmixing sediment grain size data. G-cubed 16, 4494–4506. https://doi.org/10.1002/2015GC006070.
Peck, V., Hall, I., Zahn, R., Elderfield, H., Grousset, F., Hemming, S., Scourse, J.D., 2006. High resolution evidence for linkages between NW European ice sheet instability and Atlantic Meridional Overturning Circulation. Earth Planet Sci. Lett. 243, 476–488. https://doi.org/10.1016/j.epsl.2005.12.023.
Peck, V.L., Hall, I.R., Zahn, R., Grousset, F.E., Hemming, S.R., Scourse, J.D., 2007. The relationship of Heinrich events and their European precursors over the past 60 ka BP: a multi-proxy ice-rafted debris provenance study in the North East Atlantic. Quat. Sci. Rev. 26, 862–875. https://doi.org/10.1016/j.quascirev.2006.12.002.
Peters, J., Benetti, S., Dunlop, P., Ó Cofaigh, C., 2015. Maximum extent and dynamic behaviour of the last British Irish Ice Sheet west of Ireland. Quat. Sci. Rev. 128, 48–68. https://doi.org/10.1016/j.quascirev.2015.09.015.
Peters, J., Benetti, S., Dunlop, P., Ó Cofaigh, C., Moreton, S.G., Wheeler, A., Clark, C., 2016. Sedimentology and chronology of the advance and retreat of the last British-Irish ice sheet on the continental shelf west of Ireland. Quat. Sci. Rev. 140, 101–124. https://doi.org/10.1016/j.quascirev.2016.03.012.
Pollard, R.T., Griffiths, M.J., Cunningham, S.A., Read, J.F., Perez, F.F., Rioz, A.F., 1996. Vivaldi 1991 - a study of the formation, circulation and ventilation of Eastern North atlantic waters. Prog. Oceanogr. 37, 167–192. https://doi.org/10.1016/S0079-6611(96)00008-0.
Praeg, D., Mccarron, S., Dove, D., Ó Cofaigh, C., Scott, G., Monteys, X., Facchin, L., Romeo, R., Coxon, P., 2015. Ice sheet extension to the Celtic Sea shelf edge at the last glacial maximum. Quat. Sci. Rev. 111, 107–112. https://doi.org/10.1016/j.quascirev.2014.12.010.
Prins, M., Weltje, G., 1999. End-member modeling of siliciclastic grain-size distributions: the late quaternary record of eolian and fluvial sediment supply to the arabian Sea and its paleoclimatic significance. In: Harbaugh, J.W., Watney, W.L., Rankey, E.C., Slingerland, R., Goldstein, R.H., Franseen, E.K. (Eds.), Numerical Experiments in Stratigraphy: Recent Advances in Stratigraphic and Sedimentologic Computer Simulations, vol. 62. SEPM Society for Sedimentary Geology. https://doi.org/10.2110/pec.99.62.0091, 91-11.
Prins, M.A., Bouwer, L.M., Beets, C.J., Troelstra, S.R., Weltje, G.J., Kruk, R.W., Kuijpers, A., Vroon, P.Z., 2002. Ocean circulation and iceberg discharge in the glacial North Atlantic: inferences from unmixing of sediment size distributions. Geology 30, 555–558. https://doi.org/10.1130/0091-7613(2002)030%3C0555:OCAIDI%3E2.0.CO;2.
Purcell, C., 2014. Late Quaternary Glaciation of the Continental Shelf Offshore of NW Ireland. Unpublished Masters Thesis, Durham University. http://etheses.dur.ac.uk/10774/.
Purcell, C., 2018. Fingerprinting Ice-Rafted Detritus Ice Stream Sources in the Northeast Atlantic during the Last Glacial Stage. Unpublished PhD thesis. Bangor University. https://research.bangor.ac.uk/portal/files/22069405/2018_Purcell_C_PhD.pdf.
Rea, B., Newton, A., Lamb, R.M., Harding, R., Bigg, G.R., Rose, P., Spagnolo, M., Huuse, M., Cater, J., Archer, S., Buckley, F., Halliyeva, M., Huuse, J., Cornwell, D.G., Brocklehurst, S., Howell, J., 2018. Extensive marine-terminating ice sheets in Europe from 2.5 million years ago. Sci. Adv. 4. https://doi.org/10.1126/sciadv.aar8327.
Reimer, P.J., McCormac, F.G., Moore, J.C., McCormick, F., Murray, E.V., 2002. Marine radiocarbon reservoir corrections for the midto late Holocene in the eastern subpolar North Atlantic. Holocene 12, 129–135. https://doi.org/10.1191/0959683602hl528rp.
Roberts, D.H., Evans, D., Callard, S., Clark, C., Bateman, M., Medialdea, A., Dove, D.,

Cotterill, C., Saher, M.H., Ó Cofaigh, C., Chiverrell, R., Moreton, S.G., Fabel, D., Bradwell, T., 2018. Ice marginal dynamics of the last British-Irish ice sheet in the southern north sea: ice limits, timing and the influence of the dogger bank. Quat. Sci. Rev. 198, 181–207. https://doi.org/10.1016/j.quascirev.2018.08.010.

Roberts, D.H., Grimoldi, E., Callard, L., Evans, D.J.A., Clark, C.D., Stewart, H.A., Dove, D., Saher, M., Ó Cofaigh, C., Chiverrell, R.C., Bateman, M.D., Moreton, S.G., Bradwell, T., Fabel, D., Medialdea, A., 2019. The mixd bed glacial landform imprint of the North Sea Lobe in the western North Sea. Earth Surf. Process. Landforms 44, 1233–1258. https://doi.org/10.1002/esp.4569.

Roberts, D.H., Ó Cofaigh, C., Ballantyne, C.K., Burke, M.J., Chiverrell, R.C., Evans, D.J.A., Clark, C.D., Duller, G.A.T., Ely, J.C., Fabel, D., Small, D.L., Smedley, R.K., Callard, S.L., 2020. The deglaciation of the western sector of the Irish Ice Sheet from the inner continental shelf to its terrestrial margin. Boreas 49, 438–460. https://doi.org/10.1111/bor.12448.

Roy, S., Georgiopoulou, A., Benetti, S., Sacchetti, F., 2020. Mass transport deposits in the donegal barra fan and their association with British–Irish ice sheet dynamics. Geol. Soc. Lond. Sp. Publ. 500, 567–586. https://doi.org/10.1144/SP500-2019-177.

Rüggeberg, A., Dorschel, B., Dullo, W.-C., Hebbeln, D., 2005. Sedimentary patterns in the vicinity of a carbonate mound in the hovland mound province, northern porcupine Seabight. In: Freiwald, A., Roberts, J.M. (Eds.), Cold-water Corals and Ecosystems. Springer, Berlin Heidelberg, pp. 87–112. https://doi.org/10.1007/3-540-27673-4_5.

Rüggeberg, A., Dullo, W.-C., Dorschel, B., Hebbeln, D., 2007. Environmental changes and growth history of a cold-water carbonate mound (Propeller Mound, Porcupine Seabight). Int. J. Earth Sci. 96, 57–72. https://doi.org/10.1007/s00531-005-0504-1.

Sacchetti, F., Benetti, S., Ó Cofaigh, C., Georgiopoulou, A., 2012. Geophysical evidence of deep-keeled icebergs on the Rockall bank, northeast atlantic ocean. Geomorphology 159–160, 63–72. https://doi.org/10.1016/j.geomorph.2012.03.005.

Schulz, M., 2002. On the 1470-year pacing of Dansgaard-Oeschger warm events. Paleoceanography 17. https://doi.org/10.1029/2000PA000571, 4-1.

Scourse, J., Haapaniemi, A.I., Colmenero-Hidalgo, E., Peck, V.L., Hall, I., Austin, W., Knutz, P., Zahn, R., 2009. Growth, dynamics and deglaciation of the last British Irish ice sheet: the deep-sea ice-rafted detritus record. Quat. Sci. Rev. 28, 3066–3084. https://doi.org/10.1016/j.quascirev.2009.08.009.

Scourse, J., Hall, I., McCave, I.N., Young, J., Sugdon, C., 2000. The origin of Heinrich layers: evidence from H2 for European precursor events. Earth Planet Sci. Lett. 182, 187–195. https://doi.org/10.1016/S0012-821X(00)00241-7.

Scourse, J.D., Saher, M.H., Landeghem, K.V., Lockhart, E., Purcell, C., Callard, L., Roseby, Z.A., Allinson, B., PifDkowski, A.J., Ó Cofaigh, C., Praeg, D., Ward, S., Chiverrell, R., Moreton, S., Fabel, D., Clark, C., 2019. Advance and retreat of the marine-terminating Irish Sea Ice stream into the Celtic Sea during the last glacial: timing and maximum extent. Mar. Geol. 412, 53–68. https://doi.org/10.1016/j.margeo.2019.03.003.

Scourse, J.D., Ward, S.L., Wainwright, A., Bradley, S.L., Uehara, K., 2018. The role of megatides and relative sea level in controlling the deglaciation of the British-Irish and Fennoscandian Ice Sheets. J. Quat. Sci. 33, 139–149. https://doi.org/10.1002/jqs.3011.

Sejrup, H.P., Clark, C.D., Hjelstuen, B.O., 2016. Rapid ice sheet retreat triggered by ice stream debuttressing: evidence from the North Sea. Geology 44, 355–358. https://doi.org/10.1130/G37652.1.

Shannon, P.M., 1991. The development of Irish offshore sedimentary basins. J. Geol. Soc. Lond. 148, 181–189. https://doi.org/10.1144/gsjgs.148.1.0181.

Shannon, P.M., McDonnell, A., Bailey, W.R., 2007. The evolution of the Porcupine and Rockall basins, offshore Ireland: the geological template for carbonate mound development. Int. J. Earth Sci. 96, 21–35. https://doi.org/10.1007/s00531-006-0081-y.

Small, D.L., Benetti, S., Dove, D., Ballantyne, C.K., Fabel, D., Clark, C.D., Gheorghiu, D., Newall, J.C.H., Xu, S., 2017. Cosmogenic exposure age constraints on deglaciation and flow behaviour of a marine-based ice stream in western Scotland, 2Q 16 ka. Quat. Sci. Rev. 167, 30–46. https://doi.org/10.1016/j.quascirev.2017.04.021.

Small, D.L., Smedley, R.K., Chiverrell, R.C., Scourse, J.D., Ó Cofaigh, C., Duller, G.A.T., Mccarron, S., Burke, M.J., Evans, D.J.A., Fabel, D., Gheorghiu, D., Thomas, G.S.P., Xu, S., Clark, C.D., 2018. Trough geometry was a greater influence than climate-ocean forcing in regulating retreat of the marine-based Irish-Sea Ice Stream. Geol. Soc. Am. Bull. 130, 1981–1999. https://doi.org/10.1130/B31852.1.

Smedley, R.K., Chiverrell, R.C., Ballantyne, C.K., Burke, M.J., Clark, C.D., Duller, G.A.T., Fabel, D., McCarroll, D., Scourse, J.D., Small, D.L., Thomas, G.S.P., 2017. Internal dynamics condition centennial-scale oscillations in marine-based ice stream retreat. Geology 45, 787–790. https://doi.org/10.1130/G38991.1.

Smeulders, G.G.B., Koho, K., Stigter, H., Mienis, F., Haas, H.D., Weering, T.V., 2014. Cold-water coral habitats of Rockall and Porcupine Bank, NE atlantic ocean: sedimentary facies and benthic foraminiferal assemblages. Deep Sea Res.: Topic. Stud. Oceanogr. 99, 270–285. https://doi.org/10.1016/j.dsr2.2013.10.001.

Soulsby, R., 1997. Dynamics of Marine Sands, a Manual for Practical Applications. Thomas Telford, London.

Stalling, D., Westerhoff, M., Hege, H.-C., 2005. version 2018. http://amira.zib.de, 36.

Stanford, J.D., Rohling, E., Bacon, S., Roberts, A., Grousset, F., Bolshaw, M., 2011. A new concept for the paleoceanographic evolution of Heinrich event 1 in the North Atlantic. Quat. Sci. Rev. 30, 1047–1066. https://doi.org/10.1016/j.quascirev.2011.02.003.

Stuiver, M., Reimer, P.J., 1993. Extended 14C data-base and revised calib. 3.0 C-14 age calibration program. Radiocarbon 35, 215–230. https://doi.org/10.1017/S0033822200013904.

Stuut, J., Kasten, S., Lamy, F., Hebbeln, D., 2007. Sources and modes of terrigenous sediment input to the Chilean continental slope. Quat. Int. 161, 67–76. https://doi.org/10.1016/j.quaint.2006.10.041.

Syvitski, J., Andrews, J., Dowdeswell, J., 1996. Sediment deposition in an iceberg-dominated glacimarine environment, East Greenland: basin fill implications. Global Planet. Change 12, 251–270. https://doi.org/10.1016/0921-8181(95)00023-2.

Tarlati, S., Benetti, S., Callard, S.L., Ó Cofaigh, C., Dunlop, P., Georgiopoulou, A., Edwards, R., Landeghem, K.V.V., Saher, M., Chiverrell, R., Fabel, D., Moreton, S., Morgan, S., Clark, C., 2020. Final deglaciation of the Malin Sea through meltwater release and calving events. Scot. J. Geol. 56, 117–133. https://doi.org/10.1144/sjg2019-010.

Thierens, M., Pirlet, H., Colin, C., Latruwe, K., Vanhaecke, F., Lee, J.R., Stuut, J.-B.W., Titschack, J., Huvenne, V.A.I., Dorschel, B., Wheeler, A.J., Henriet, J.-P., 2012. Ice-rafting from the British-Irish ice sheet since the earliest Pleistocene (2.6 million years ago): implications for long-term mid-latitudinal ice-sheet growth in the North Atlantic region. Quat. Sci. Rev. 44, 229–240. https://doi.org/10.1016/j.quascirev.2010.12.020.

Thierens, M., Titschack, J., Dorschel, B., Huvenne, V.A.I., Wheeler, A.J., Stuut, J.-B.W., O'Donnell, R., 2010. The 2.6 Ma depositional sequence from the Challenger cold-water coral carbonate mound (IODP Exp. 307): sediment contributors and hydrodynamic palaeo-environments. Mar. Geol. 271, 260–277. https://doi.org/10.1016/j.margeo.2010.02.021.

Titschack, J., Baum, D., De Pol-Holz, R., López Correa, M., Forster, N., Flögel, S., Hebbeln, D., Freiwald, A., 2015. Aggradation and carbonate accumulation of Holocene Norwegian cold-water coral reefs. Sedimentology 62, 1873–1898. https://doi.org/10.1111/sed.12206.

Tjallingii, R., Claussen, M., Stuut, J., Fohlmeister, J., Jahn, A., Bickert, T., Lamy, F., Röhl, U., 2008. Coherent high- and low-latitude control of the northwest African hydrological balance. Nat. Geosci. 1, 670–675. https://doi.org/10.1038/ngeo289.

Toucanne, S., Soulet, G., Freslon, N., Jacinto, R., Dennielou, B., Zaragosi, S., Eynaud, F., Bourillet, J.-F., Bayon, G., 2015. Millennial-scale fluctuations of the European Ice Sheet at the end of the last glacial, and their potential impact on global climate. Quat. Sci. Rev. 123, 113–133. https://doi.org/10.1016/j.quascirev.2015.06.010.

van Ledden, M., Kesteren, W.G.M.v., Winterwerp, J.C., 2004. A conceptual framework for the erosion behaviour of sand-mud mixtures. Continent. Shelf Res. 24, 1–11. https://doi.org/10.1016/j.csr.2003.09.002.

van Rooij, D., Blamart, D., Richter, T.O., Wheeler, A.J., Kozachenko, M., Henriet, J.-P., 2007. Quaternary sediment dynamics in the Belgica mound province, Porcupine Seabight: ice-rafting events and contour current processes. Int. J. Earth Sci. 96, 121–140. https://doi.org/10.1007/s00531-006-0086-6.

Wadham, J., Hawkings, J., Tarasov, L., Gregoire, L., Spencer, R., Gutjahr, M., Ridgwell, A., Kohfeld, K., 2019. Ice sheets matter for the global carbon cycle. Nat. Commun. 10. https://doi.org/10.1038/s41467-019-11394-4.

Ward, S.L., Scourse, J.D., Yokoyama, Y., Neill, S.P., 2020. The challenges of constraining shelf sea palaeotidal models using sediment grain size as a proxy for tidal currents. Continent. Shelf Res. 205, 104165. https://doi.org/10.1016/j.csr.2020.104165.

Weiser, J., Titschack, J., Kienast, M., McCave, I.N., Lochte, A.A., Saini, J., Stein, R., Hebbeln, D., 2021. Atlantic water inflow to Labrador Sea and its interaction with ice sheet dynamics during the Holocene. Quat. Sci. Rev. 256, 106833. https://doi.org/10.1016/j.quascirev.2021.106833.

Weltje, G., 1997. End-member modeling of compositional data: numerical-statistical algorithms for solving the explicit mixing problem. Math. Geol. 29, 503–549. https://doi.org/10.1007/BF02775085.

Weltje, G., Prins, M., 2003. Muddled or mixed? Inferring palaeoclimate from size distributions of deep-sea clastics. Sediment. Geol. 162, 39–62. https://doi.org/10.1016/S0037-0738(03)00235-5.

Wheeler, A., Lim, A., Peters, J., Sacchetti, F., McGrath, M., Browne, M., El Kateb, A., Ní Fhaoláin, F., Renken, S., Schiele, K., Vertino, A., Officers & Crew of the RV Celtic Explorer, 2014. West of Ireland Coring Programme (WICPro). RV Celtic Explorer. Cork – Killybegs. 6th March to 18th March 2014. Cruise Report, UCC. https://www.ucc.ie/en/media/research/marinegeo/mgpdfs/WICPro-Cruise-Report-CE14014.pdf.

White, M., Roberts, J.M., van Weering, T.C.E., 2007. Do bottom-intensified diurnal tidal currents shape the alignment of carbonate mounds in the NE Atlantic? Geo Mar. Lett. 27, 391–397. https://doi.org/10.1007/s00367-007-0060-8.

Wienberg, C., Titschack, J., Frank, N., Pol-Holz, R.D., Fietzke, J., Eisele, M., Kremer, A., Hebbeln, D., 2020. Deglacial upslope shift of NE Atlantic intermediate waters controlled slope erosion and cold-water coral mound formation (Porcupine Seabight, Irish margin). Quat. Sci. Rev. 237, 106310. https://doi.org/10.1016/j.quascirev.2020.106310.

Wilson, L.J., Austin, W., 2002. Millennial and sub-millennial-scale variability in sediment colour from the Barra Fan, NW Scotland: implications for British ice

sheet dynamics. Geol. Soc. Lond. Sp. Publ. 203, 349–365. https://doi.org/10.1144/GSL.SP.2002.203.01.18.

Wilson, L.J., Austin, W., Jansen, E., 2002. The last British Ice Sheet: growth, maximum extent and deglaciation. Polar Res. 21, 243–250. https://doi.org/10.3402/polar.v21i2.6484.

Wilson, P., Ballantyne, C.K., Benetti, S., Small, D.L., Fabel, D., Clark, C.D., 2018. Deglaciation chronology of the donegal ice centre, north-west Ireland. J. Quat. Sci. 34, 16–28. https://doi.org/10.1002/jqs.3077.

Wilton, D., Bigg, G., Scourse, J., Ely, J., Clark, C., 2021. Exploring the extent to which fluctuations in ice-rafted debris reflect mass changes in the source ice sheet: a model–observation comparison using the last British–Irish Ice Sheet. J. Quat. Sci. 36, 934–945. https://doi.org/10.1002/jqs.3273.

Woodworth, P., Melet, A., Marcos, M., Ray, R., Wöppelmann, G., Sasaki, Y.N., Cirano, M., Hibbert, A., Huthnance, J., Monserrat, S., Merrifield, M., 2019. Forcing factors affecting sea level changes at the coast. Surv. Geophys. 1–47. https://doi.org/10.1007/s10712-019-09531-1.

Woronko, B., 2016. Frost weathering versus glacial grinding in the micromorphology of quartz sand grains: processes and geological implications. Sediment. Geol. 335, 103–119. https://doi.org/10.1016/j.sedgeo.2016.01.021.

Wu, L., Wilson, D., Wang, R., Passchier, S., Krijgsman, W., Yu, X., Wen, T., Xiao, W., Liu, Z., 2020. Late quaternary dynamics of the lambert glacier-amery ice shelf system, east Antarctica. Quat. Sci. Rev. https://doi.org/10.1016/j.quascirev.2020.106738, 106738.